

Chapter 7

Cardiovascular MR Image Analysis

Milan Sonka¹, Daniel R. Thedens¹, Boudewijn P. F. Lelieveldt²,
Steven C. Mitchell¹, Rob J. van der Geest², and Johan H. C. Reiber²

¹The University of Iowa, Iowa City, USA

{milan-sonka, dan-thedens, steven-mitchell}@uiowa.edu;

²Leiden University Medical Center, Leiden, The Netherlands

{b.p.f.lelieveldt, rvdgeest, j.h.c.reiber}@lumc.nl

Summary. Magnetic resonance (MR) imaging allows 2D, 3D, and 4D imaging of living bodies. The chapter¹ briefly introduces the major principles of magnetic resonance image generation, and focuses on application of computer vision techniques and approaches to several cardiovascular image analysis tasks. The enormous amounts of generated MR data require employment of automated image analysis techniques to provide quantitative indices of structure and function. Techniques for 3D segmentation and quantitative assessment of left and right cardiac ventricles, arterial and venous trees, and arterial plaques are presented.

7.1 Introduction

Cardiovascular disease is the number one cause of death in the western world. Cardiac imaging is an established approach to diagnosing cardiovascular disease and plays an important role in its interventional treatment. Three-dimensional imaging of the heart and the cardiovascular system is now possible with x-ray computed tomography, magnetic resonance, positron emission tomography, single photon emission tomography, and ultrasound, to name just the main imaging modalities. While cardiac imaging capabilities are developing rapidly, the images are mostly analyzed visually and therefore qualitatively. The ability to quantitatively analyze the acquired image data is still not sufficiently available in routine clinical care. Large amounts of acquired data are not fully utilized because of the tedious and time-consuming character of manual analyses. This is even more so when 3D image data need to be processed and analyzed.

In this chapter, we will concentrate on cardiac image analysis that uses magnetic resonance (MR) to depict cardiovascular structure. After briefly describing capabilities of MR to image the heart and vascular system, we will

¹ Portions reprinted, with permission, from *IEEE Transactions on Medical Imaging*, Volume 21, pp. 1167–1178, September 2002. © 2002 IEEE.

devote the rest of the chapter to outlining techniques of highly automated MR image analysis.

7.2 Capabilities of MRI

Principles of MR Imaging

Magnetic resonance imaging (MRI) relies on the phenomenon of *nuclear magnetic resonance* to generate image contrast [1, 2]. The hydrogen atom (along with other species having an odd number of protons or neutrons, such as sodium and phosphorous) possess a spin angular momentum. The single proton of the hydrogen atom (often referred to in this context as a *spin*) is by far the most abundant, and thus is considered in the vast majority of imaging applications. Most importantly, for the purposes of imaging, the spins will give rise to a magnetic moment and will act like microscopic bar magnets. As a result, when the protons are placed in a strong static magnetic field, at equilibrium they tend to line up in the same direction as the external field. The net effect of all the spins lined up in this way generates a small but measurable magnetization along the longitudinal direction of the large external field. The magnitude of this magnetization increases as the strength of the external field is increased.

By itself, this magnetization does not give much useful information about the distribution of the protons within the object. The application of a second small (relative to the primary strong field) magnetic field oscillating in the radiofrequency (RF) range sets up a resonance condition and will perturb the spins away from their equilibrium state, “tilting” them away from their alignment with the main field into the transverse plane. Much like a gyroscope, this will *excite* the spins causing them (and their magnetic fields) to precess about the direction of the main field, and the rate at which the spins precess is directly proportional to the strength of the main magnetic field. Figure 7.1 shows the relationship between the two magnetic fields and the resulting perturbation of the magnetization vector. A fundamental principle of electromagnetics is that a time-varying magnetic field can induce an electric current in an appropriately placed coil of wire, generating a signal that can measure the distribution of the spins within the object. Since the rate of precession depends on the magnetic field strength, slightly varying the strength across the bore of the magnetic with *gradient* fields yields a spatially varying rate of precession [3]. When the RF field is removed, the spins begin to return towards their equilibrium state aligned with the strong static magnetic field.

The rate of return of spins to their equilibrium state is governed by two time constants intrinsic to different tissue types, T1 and T2. T2 determines how long it will take for the signal generated by the “tipped” spins to decay away. T1 measures the amount of time it takes for the spins to completely return to their equilibrium alignment with the main magnetic field (see Figure

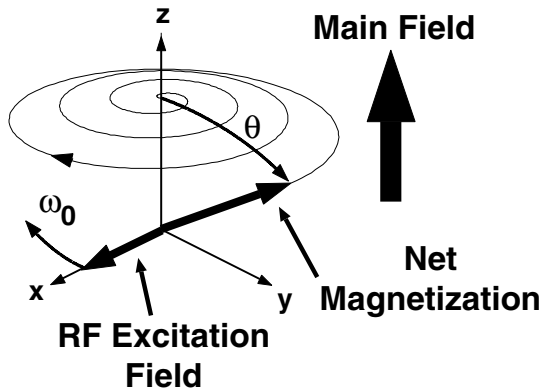


Figure 7.1. Generation of MRI signal with RF field. Application of a small rotating magnetic field at the resonant frequency ω_0 causes the magnetization vector to tilt and precess into the transverse ($x-y$) plane by an angle θ . The precessing transverse component generates the MR signal, which can be detected by a receiver coil.

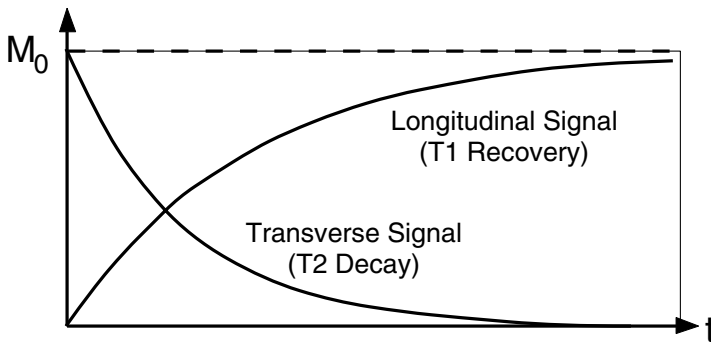


Figure 7.2. Relaxation of transverse and longitudinal magnetization. After excitation, the measurable transverse signal decays away with time constant T_2 , while the longitudinal magnetization is recovered with a time constant T_1 . Both constants are dependent on tissue type and strength of the main field.

7.2. Because of this signal decay, an MR imaging experiment generally must consist of several cycles of signal generation followed by signal measurement or acquisition.

Hence, the signal measured from a tissue will depend on its density of protons as well as its T_1 and T_2 relaxation parameters. Motion and flow also contribute to the final signal generated. The remarkable ability of MRI to generate a wide variety of tissue contrast arises from the fact that the imaging experiment can be designed to vary the relative weight of each of these parameters in the measured signal. For example, muscle and fat have very different T_1 and T_2 parameters and by varying the timing of the applied RF

excitation pulses, maximum contrast between the two can be achieved. Other strategies may enhance or suppress flowing blood compared to stationary tissues.

Challenges of Cardiovascular MRI

Cardiovascular imaging presents formidable challenges for any imaging modality as well as some unique to MRI. Because the signal generated by a single RF excitation decays away quite rapidly (on the order of milliseconds), formation of a complete image nearly always requires repeated excitations and data acquisition. Motion of tissues between acquisitions or during a single acquisition causes blurring and other artifacts that compromise image quality. The heart is in constant motion throughout the cardiac cycle, and respiration also causes the heart and other organs of the chest and abdomen to shift positions throughout duration of an image acquisition. Both types of motion must be suppressed in some way if high-resolution images of the cardiovascular anatomy are to be generated.

The problem of cardiac motion is overcome by synchronizing each excitation and data acquisition to the heart cycle, as measured by electrocardiography [4]. Each data acquisition is acquired during a narrow window of time at the same point or phase of the heart cycle, yielding a correctly registered set of measurements that can be reconstructed with minimal motion artifact. The drawback is that only a fraction of each heart cycle can be utilized for data collection, causing a concomitant increase in the time required to acquire an image. This time can be used to acquire images from the same or other locations at different points within the heart cycle without an additional time penalty, however.

Respiratory motion is generally not as predictable as cardiac motion and occurs over a different time scale. Three basic strategies have been used to overcome image degradations. For relatively rapid two-dimensional techniques that can be acquired in fewer than 15 to 20 heartbeats, subjects are instructed to hold their breath for the duration of the scan. Longer scans can be achieved with repeated breath-holding, though this requires a consistent breath-hold position on the part of the subject to achieve optimal results. Respiratory triggering is another option, whereby data are acquired only during a limited part of the respiratory cycle (analogous to cardiac triggering). A more sophisticated method for lengthy 2D and 3D acquisitions is navigator gating [5, 6]. For each image data acquisition, an additional set of pulses determines the position of the diaphragm and adjusts the imaging plane and data acquisition to minimize or track this motion. This permits high-resolution and artifact-free images while the subject breathes freely.

Recently developed real-time imaging strategies can acquire a complete image in a matter of milliseconds, eliminating the need for either type of motion suppression [7]. Such techniques still remain limited in the resolution

and signal-to-noise ratio (SNR) that can be achieved and cannot yet replace the more time-consuming scan protocols.

Cardiac Morphology

The most basic use of cardiac MRI is to depict the structure or morphology of the heart. Two general classes of imaging techniques are widely used for cardiac imaging, commonly referred to as black-blood and bright-blood techniques.

Black-Blood Imaging. Black-blood images are produced by T2-weighted spin-echo (SE) imaging sequences, in which two RF excitations (an excitation pulse and an inversion pulse) are applied to the imaged volume [4]. After the excitation pulse, the excited spins begin to lose coherence due to slight variations in their resonant frequencies, resulting in a rapid loss of overall signal. The inversion pulse “flips” the magnetization about one of the axes permitting these spins to regain their coherence and generate an *echo* when the signal has been restored. When the two pulses are separated by a sufficient interval, flowing blood experiences only one of these pulses and thus does not produce a restored signal echo, leaving a flow void in the chambers of the heart. The timing of the two RF pulses sets the echo time (TE) at which the signal refocuses (and data are acquired) and determines the precise signal and contrast features of the image. For black blood imaging, a TE of at least 20 msec is usually used. A longer TE yields greater contrast based on T2 characteristics of the tissues, which may be useful to identify such lesions as acute myocardial infarction or myocardial scar. This comes at the expense of reduced overall signal due to signal decay. Standard SE sequences show excellent contrast among myocardium (medium intensity), epicardial fat (high intensity), and flowing blood (low intensity). The signal void created by SE sequences generates images with especially good contrast in endocardial regions, valves, and vessel walls.

The main limitation of standard SE sequences is the acquisition time required in a cardiac-triggered exam, which results in poor temporal resolution and the prospect of significant respiratory motion artifact. Fast SE (FSE) sequences overcome this limitation by applying multiple inversion pulses and additional signal readouts during a single cardiac cycle. Speedups of an order of magnitude are possible in this way. However, the longer readout times degrade the image contrast due to the more complex dependence on relaxation times.

The currently preferred black-blood technique for imaging cardiac morphology is a T2-weighted inversion recovery (IR) pulse sequence [8]. This sequence applies additional RF excitation pulses to effectively null the signal from blood (and possibly fat as well) based on its T1 relaxation parameters. This is usually followed by a FSE sequence that can be acquired in 15 to 20 heartbeats, suitable for a breath-held acquisition and yielding a robust black-blood sequence with T2 contrast.

Bright-Blood Imaging. Bright-blood images originate from gradient echo (GRE) imaging sequences which only use a single RF excitation, relying on the gradient hardware instead of an inversion pulse to refocus the signal for data acquisition. Much shorter TE times (1–10 msec) are used, and the excitation and data readouts can be repeated more frequently (every 10–20 msec). Because blood need only experience the single RF pulse to generate a signal, it appears brighter than myocardium on GRE acquisitions. The short TE between excitation and data readout enhances this effect since there is less time for signal decay due to relaxation. Additional flow-compensation pulses can also be applied to further enhance blood signal and improve contrast with nearby myocardium. As with FSE imaging, the fastest imaging sequences utilize multiple excitations and data readouts over an extended interval (80 msec is a typical duration) synchronized to the cardiac cycle to generate images that can be acquired within a breath-holding interval [9]. Contrast between blood and myocardium is generally not as good as with SE imaging, as varying flow profiles may result in heterogeneous blood pool.

The availability of faster gradient hardware has seen a resurgence of techniques based on steady-state free precession (SSFP) [10]. SSFP maximizes the use of signal from blood by applying rapid excitations repeated at very short intervals. The resulting contrast is a function of relaxation parameters as T_1/T_2 . The short repetition times greatly reduce flow effects and show a more homogeneous depiction of myocardial blood pool, which in turn improves contrast with myocardium and visualization of papillary muscles. Rapid excitations also permit better temporal resolution [11, 12], or the time savings can be traded off for higher resolution at the same time resolution. As state-of-the-art MR gradient hardware proliferates, SSFP will likely become even more common.

The rapid repetition of readouts in both GRE and SSFP mean that several images at the same location can be taken at different time points within the heart cycle. Alternatively, the imaging time can be used to acquire multiple slices at a reduced temporal resolution. Using segmented acquisitions, a multi-slice multiphase view of the cardiac morphology can be acquired within a single breath-hold of 15 to 20 heartbeats.

Cardiac Function

Many of the techniques mentioned above for imaging of cardiac morphology, including both black-blood and bright-blood imaging, are also suitable for measuring cardiac function indices as well. Compared to other modalities, MRI has the advantage that completely arbitrary image orientations can be chosen, guaranteeing that true long-axis or short-axis views serve as the basis for quantitative measurements. The availability of three-dimensional information in the form of multiple parallel slices eliminates the need for any geometric assumptions about ventricular anatomy when estimating masses and volumes, a significant advantage over x-ray and ultrasound.

Bright-blood GRE imaging is more commonly used for evaluation of ventricular function. The shorter acquisition time permits a greater number of slices to be acquired during the cardiac cycle, which can be used for higher temporal resolution (more frames per cycle) or for a greater volume coverage (more slice locations). The acquisition of images at multiple phases of the cardiac cycle is known as cine MRI (example shown later in Figure 7.8) [13]. With present system hardware, a complete multislice multiphase cine data set suitable for quantitative analysis can be acquired in a single breath-hold interval. The limiting factor with standard GRE imaging is the contrast between medium-intensity myocardium and the bright blood pool. Areas of slower flowing blood will demonstrate reduced intensity making delineation of the endocardial contours difficult.

The recent advances in SSFP imaging cited above may solve this problem to some degree with its more robust contrast. The faster repetition time used in SSFP also increases the frame rates possible in a cine study. With state-of-the-art gradient hardware, truly 3D cine MRI with no gaps between slices is now possible within a single breath-hold interval [14, 15].

Improving gradient and computing hardware has now made real-time imaging feasible for functional imaging. Rates of 16 frames per second or more can be continuously obtained much like x-ray fluoroscopy [7]. The scan plane can be modified directly on the real-time images, dramatically reducing the time required for “scout” scans to find the proper short-axis orientation. At such rates, cardiac gating and breath-holding are unnecessary, which permits imaging of patients with arrhythmias. Presently, spatial resolution of real-time studies remain comparatively limited, but a number of ongoing developments in image reconstruction techniques are improving this. Two such strategies exploit the widespread use of multiple receiver coils. Simultaneous acquisition of spatial harmonics (SMASH) [16] and sensitivity encoding (SENSE) [17] use the spatially varying response of a group of coils as an additional means of spatial encoding to reduce the time needed to acquire a given resolution image. Other techniques analyze the temporal dimension of the acquisition to reduce the acquisition of redundant information and enhance either temporal or spatial resolution [18].

Each of these forms of cine and real-time MRI data are useful for computing several global measures of cardiac function. Accurate and reproducible quantitative measurements of ventricular volumes at both systole and diastole, masses, and ejection fraction (difference between the diastolic and systolic ventricular volumes) are all computable with multislice or volume data sets. In each case, myocardial border identification is necessary to extract quantitative results. Compared to x-ray and ultrasound, MRI also accurately depicts epicardial borders, again eliminating the geometric assumptions that often must be made in competing modalities. As a result, regional myocardial function assessments can also be made with cine techniques. This may be done subjectively viewing cine or real-time “loops” or through quantitative measurements of regional wall thickness and strain.

Regional measurements of three-dimensional strain is possible using myocardial tagging. This imaging method excites myocardium with a pattern of lines or grids whose motion can then be tracked over the heart cycle, providing a precise depiction of the deformations occurring within the myocardial tissues. Analysis of these deformations in short- and long-axis views gives 3D strain measurements useful for determining local myocardial function. A promising rapid technique is harmonic phase (HARP) imaging which has potential as a real-time technique [19].

Myocardial Perfusion

Another important indicator that can be assessed by MRI is regional blood flow (or perfusion) in the myocardium. This may indicate areas of damage to myocardium from a cardiac event or insufficient blood flow resulting from a significant arterial stenosis. Determination of blood flow within the myocardium depends on the use of contrast agents (usually gadolinium-based) that change the relaxation characteristics of blood, particularly the T1 relaxation time [20]. Gadolinium causes a considerable shortening of the T1 relaxation time, meaning that magnetization returns to equilibrium much more rapidly. As shown in Figure 7.3, when RF excitation pulses are applied in rapid succession, tissues with short T1 relaxation will still have time to recover and generate greater signal for subsequent excitations. Longer T1 relaxation times means that little magnetization has returned to the equilibrium state, so later excitations result in much less signal. Appropriate timing of a pair of RF pulses can maximize the signal difference between two tissues with known T1 relaxation times.

Perfusion is mostly measured during the “first pass” into the myocardium after injection of contrast agent [21, 22]. Areas of myocardium with adequate blood flow will have enhanced intensity from the shortened T1 of the inflowing blood. Perfusion deficits will not receive this material and remain at lower intensity. The time of the imaging window is limited as contrast material may soon begin to diffuse from normal to deficit regions, and the contrast agent will recirculate with the blood within 15 seconds. Hence, rapid GRE sequences are used to image quickly and permit multiple slices to be obtained over a volume. T1 contrast is maximized by applying an RF “preparation” pulse that initially excites or saturates all of the blood and tissues. After a delay time that causes contrast-enhanced material to return towards equilibrium while the longer T1 tissues recover much less magnetization to yield strong T1 contrast, a standard fast GRE imaging sequence is applied. The result is bright signal in normal tissue and low-intensity regions of perfusion deficit. Acquisition of several time frames during this process permits quantitative measurements of the severity of these perfusion abnormalities.

Further myocardial tissue characterization is possible using gadolinium contrast agents by waiting a considerable duration (20 min or more) before imaging [22, 23]. Gadolinium contrast will eventually move to the extracellular

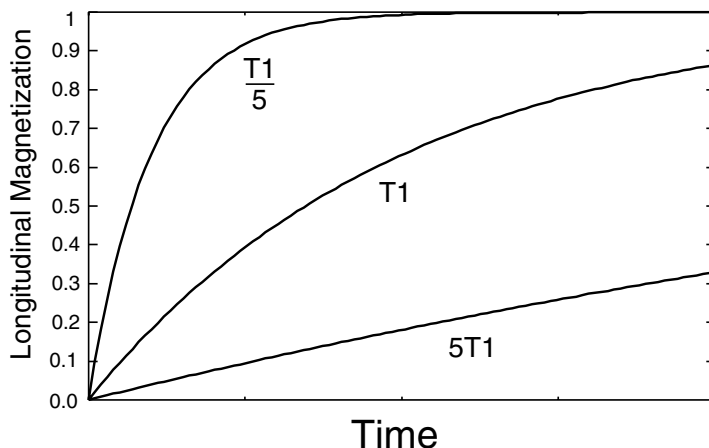


Figure 7.3. Generation of T1-based contrast. A typical RF excitation causes the longitudinal magnetization to go to zero, followed by recovery via T1 relaxation. The amount of recovery depends on the T1 time constant and determines the amount of signal available for imaging during the next excitation. When the repetition time is brief, short T1 species will recover and generate much greater signal than longer T1 species.

space and accumulate more in areas of nonviable myocardium, resulting in enhanced signal in these areas on T1 weighted images compared to normal tissue.

Angiography

In addition to imaging of the heart, MRI has also been widely applied to imaging vessels throughout the body. Its advantages over conventional X-ray angiography go beyond the fact that it is much less invasive. MRI can also collect true 3D data, permitting arbitrary selection of views and slices in post-processing to optimize the visualization of vessels. This is especially helpful in complex vascular trees where tracing the vessel of interest may be difficult. Contrast for MR angiography can be developed in two ways. Pulse sequences may exploit the different signal properties of flowing and stationary tissues to produce images. Other sequences rely on the relaxation characteristics of arterial and venous blood, usually enhanced by T1-shortening contrast agents as described for myocardial perfusion. In both cases, the goal is to generate images of the vessel lumen suitable to detect and evaluate stenoses.

Two flow-based imaging techniques are in common use for MR angiography and both effectively produce “bright-blood” images of the vessel lumen. Phase-contrast (PC) imaging takes advantage of the fact that flowing blood will move during the data acquisition readout. Since spatial information is

encoded by a spatially varying magnetic field gradient, flowing spins experience a changing magnetic field as they move, resulting in a phase change in their signal compared to stationary tissues. By applying an appropriate encoding gradient pattern prior to imaging, flowing blood can be selectively viewed. PC imaging can also quantitatively measure flow velocities. Time-of-flight (TOF) imaging uses the continuous replacement of flowing blood in the imaged slice to differentiate it from static tissue. Rapid repetition of excitation pulses covering the imaged slice saturates and eventually eliminates signal from stationary material because there is not enough time to regain any equilibrium magnetization. Flowing blood retains a signal since fresh unsaturated blood is constantly flowing into the slice to be excited and flows away again before saturation can be complete. The result produces high signal from flowing blood against the low intensity of background structures.

Reliance on flow for image contrast may introduce artifacts where flow patterns are not ideal. Such anomalies will affect both PC and TOF sequences. Areas of slow flow may have reduced signal, either due to reduced phase changes for PC or saturation in TOF. Complex flow patterns and turbulence can also cause reduced intensities within the vessel lumen in both cases. The consequences could include stenoses that are overestimated or a false appearance of an occlusion of the vessel.

The limitations of flow-based angiography have made flow-independent techniques more prevalent. It is possible to create high-contrast angiographic images using only the intrinsic T1 and T2 relaxation characteristics of blood using a variety of “prepared contrast” pulses that saturate or suppress one or more background tissues [24]. However, injectable contrast agents such as those based on gadolinium compounds have proven to be safe and well tolerated and are widely available. These contrast agents dramatically reduce the T1 relaxation time of blood and greatly enhance its signal on TOF images. Much of MR angiography is now dominated by contrast-agent-based protocols.

Once again, the main limiting factor in contrast studies is the time before the contrast agent leaks outside the blood vessels and begins to enhance the signal in tissues other than blood. Successful contrast angiography therefore requires careful timing of contrast injection and image acquisition and a rapid acquisition technique to minimize artifacts due to contrast dispersion and respiratory motion. Fast 3D GRE imaging is most commonly used to acquire the T1-based contrast to yield bright contrast-enhanced blood pool. Subtraction of a non-contrast-enhanced volume may also be used to further suppress background structures. A variety of strategies have been employed to reduce the imaging time to acquire a 3D data set even further and assure accurate timing of the acquisition. Partial acquisition methods which acquire 60–75% of a full data set and synthesize the rest based on mathematical assumptions can help reduce imaging times. More extreme versions of this have been applied to radial sampling patterns to reduce acquisition time even further, trading the shortened time for some increased and coherent background noise [25].

The timing of the acquisition relative to the injection of contrast agent is also crucial. If the data acquisition occurs too early, the signal will not yet be enhanced, while a late acquisition will show poor contrast because of a heightened signal from other tissues or veins. For many applications, a fixed time delay based on previous experience may be sufficient, although increased doses of contrast often accompany this technique to increase the window of enhancement. A much smaller dose of contrast may be given and tracked with a sequence of rapid 2D images used to pinpoint the transit time prior to a full 3D acquisition. Automatic monitoring of the signal at a predefined location upstream from the desired location has also been implemented. The use of real-time imaging to monitor contrast passage is another possibility.

The limited volume imaging time available because of the dispersion of contrast agent into other tissues is currently being addressed. New intravascular contrast agents that do not leak into tissues during the course of a typical MR exam are being perfected by a number of researchers [26, 27]. As a result, their T1 shortening properties can be utilized for longer or multiple exams without the enhancement of background tissues. MR angiograms in higher-resolution 3D or over the whole body then become possible. The longer persistence in the blood pool does mean that both arteries and veins will be displayed for longer 3D scan durations. Some means of separating the two may be needed for diagnostic use of such images.

Coronary artery imaging may be a particular beneficiary of such contrast agents, as the necessity of high-resolution, 3D coverage, and motion correction requires longer scan times than are feasible with standard contrast material. The flow and saturation effects that often compromise 3D techniques are also improved with such contrast agents [28]. Perfection of a minimally invasive coronary MR imaging is of particular interest because of the number of highly invasive x-ray angiography procedures that are performed that show no clinically significant disease.

In summary, MR imaging shows tremendous promise to assess virtually all areas of cardiovascular health. While the much-heralded ascendance of MRI as the “one-stop shop” for noninvasive cardiovascular imaging has not yet come to pass, the current state-of-the-art and continued advances in cardiac MRI still point towards such a possibility.

7.3 Cardiac MR Segmentation

The rapid development of cardiac magnetic resonance (MR) acquisition techniques as described in the previous section has created a vast diagnostic potential, and within one patient examination, several aspects of cardiac function can be evaluated. A major bottleneck for cardiac MR methods in routine clinical practice however, is the prohibitively large amount of data involved in a comprehensive patient examination (typically between 2000 and 5000 images). Therefore, to utilize the full diagnostic potential of cardiac MR, highly

automated quantitative analysis is essential; hence image segmentation is of primary importance to further advance the clinical utility of cardiac MR.

Though much effort has been directed to automated segmentation of cardiac MRI image data, there are three main reasons why existing methods frequently exhibit a lower success rate in comparison with human expert observers, especially when applied to clinical-quality images — existing methods do not incorporate a sufficient amount of a priori knowledge about the segmentation problem; do not consider 3D or temporal context as an integral part of their functionality; and position the segmentation boundaries at locations of the strongest local image features not considering true anatomical boundary locations.

7.3.1 Cardiac Segmentation Approaches

A number of 3D medical image analysis approaches occurred recently, many of them addressing one or more of the above-mentioned shortcomings of available segmentation techniques. A detailed review of existing 3D cardiac modeling approaches is provided in [29]. In the context of our work and considering the goal of segmenting 3D volumetric and temporal cardiac images and image sequences, statistical modeling of 3D shape and 3D image properties is crucial. Vemuri and Radisavljevic concentrated on a 3D model that combines deformed superquadric primitives with a local displacement field expressed on an orthonormal wavelet basis [30]. As a result of this orthonormal basis, the shape parameters become physically meaningful, and thus a preferred shape can be imposed based on parameter distributions in a set of training samples. Similarly, Staib and Duncan developed a 3D balloon model [31]. The model is parameterized on an orthonormal Fourier basis such that the statistics of the Fourier coefficients in a training set allow a constrained image search. Model fitting in these two methods is performed by balancing an internal energy term with an external, gradient derived, scalar field. Metaxas et al. introduced physics-based deformable models for modeling rigid, articulated, and deformable objects, their interactions with the physical world, and the estimate of their shape and motion from visual data [32, 33].

Cootes and Taylor and colleagues developed a statistical point distribution model (PDM) and demonstrated its utility for 2D image segmentation [34, 35]. One of the primary contributions was an ease of automated learning of the model parameters from sets of corresponding points as well as the PDM's ability to incorporate shape and boundary gray level properties and their allowed variations. Applications to segmentation of echocardiographic data [36] and deep neuroanatomical structures from MR images of the brain may serve as examples [37]. Following the point distribution model ideas, Kelemen et al. built a statistical model of 3D shapes using parametric surface representations [38]. Similar to PDMs, shape and gray level information in the boundary vicinity was incorporated in the model. The method's performance

was demonstrated on 3D segmentation of neuroanatomical structures. A multiscale 3D shape modeling approach called M-reps was developed by Pizer et al. [39]. M-reps support a coarse-to-fine hierarchy and model shape variations via probabilistically described boundary positions with width- and scale-proportional tolerances. Three-dimensional echocardiographic image segmentation using core atoms was reported by Stetten and Pizer[40]. Davatzikos et al. presented a deformable model in which geometric information is embedded via a set of affine-invariant attribute vectors; these vectors characterize the geometric structure around a model point from a local to global scale, forming an adaptive focus deformable statistical shape model [41]. The methodology was applied to segmentation of neuroanatomical structures.

In all the above-referenced approaches, the models primarily hold information about shape and its allowed variations. The information about image appearance is only considered in a close proximity to the object borders. A powerful, model driven segmentation technique called active appearance model (AAM) was recently introduced by Cootes and coworkers [42, 43, 44]. An AAM describes the image appearance and the shape of an object in a set of examples as a statistical shape-appearance model. AAMs can be applied to image segmentation by minimizing the difference between the model and an image along statistically plausible shape/intensity variations (analysis by synthesis). AAMs have been shown to be highly robust in the segmentation of routinely acquired single-phase, single-slice cardiac MR [45] and echo images [46], because they exploit prior knowledge about the cardiac shape, image appearance, and observer preference in a generic way. For a detailed background on active appearance models and their application to image segmentation, the reader is referred to [43].

Two-dimensional active appearance motion models [45, 47, 46] have demonstrated the ability of time-continuous segmentation by exploiting temporal coherency in the data. However, these 2D + time AAMs do not represent a true 3D approach. Their segmentation ability is limited to cases with fixed numbers of preselected frames; they rely on a priori knowledge of image frame correspondences within each cardiac cycle. The 3D model presented below is the first such to date capable of successful segmentation of cardiac MR images [48]. The model's behavior is learned from manually traced segmentation examples during an automated training stage. The shape and image appearance of the cardiac structures are contained in a single model. This ensures a spatially and/or temporally consistent segmentation of three-dimensional cardiac images.

Point Distribution Model Concept

Point distribution models describe populations of shapes using statistics of sets of corresponding landmarks of the shape instances [34, 35, 49]. By aligning N shape samples (consisting of n landmark points) and applying a principal component analysis (PCA) on the sample distribution, any sample \mathbf{x}

within the distribution can be expressed as an average shape $\bar{\mathbf{x}}$ with a linear combination of eigenvectors P superimposed

$$\mathbf{x} = \bar{\mathbf{x}} + P\mathbf{b}. \quad (7.1)$$

In 2D models, $p = \min(2n, N - 1)$ eigenvectors P form the principal basis functions, while in a 3D model; $p = \min(3n, N - 1)$ eigenvectors are formed. (The minimum operator is needed since we frequently have more corresponding shape points than training set samples.) In both cases the corresponding eigenvalues provide a measure for compactness of the distribution along each axis. By selecting the largest q eigenvalues, the number of eigenvectors can be reduced, where a proportion k of the total variance is described such that

$$\sum_{i=1}^q \lambda_i \geq k \cdot \text{Total} \quad \text{where} \quad \text{Total} = \sum_{i=1}^p \lambda_i. \quad (7.2)$$

7.3.2 Representing the Shape of 3D Cardiac Ventricles

Extending the 2D PDM to three dimensions is a nontrivial task. In order to create a compact and specific model, point correspondences between shapes are required. Even if landmark points are easily identifiable in both models, specifying a uniquely corresponding boundary surface built from points in between these landmarks is difficult in 3D. In a 2D case [45], a boundary sequence of points may be identified by evenly sampling points spanning from one landmark to the next. In a 3D case, defining a unique sampling of the object surfaces is ill-posed but the problem can be solved in simplified geometries. An approach like that was used for left-ventricular segmentation.

For the purpose of ventricular segmentation, a normalized cylindrical coordinate system is defined with its primary axis aligned with the long axis of the heart, and the secondary axis aligned with the posterior junction of the right and left ventricles in the basal slice. The cardiac ventricles resemble a cylindrical or paraboloid shape. First, contours are sampled slice-by-slice at even angle increments. To transform the rings in the normalized cylindrical coordinate system, each point on the ring is connected by a straight line to the next adjacent corresponding point on the rings above and below. Starting from the apex slice to the basal slice, a fixed number of slicing planes are placed evenly along the long axis. Apex slice was defined as the most inferior slice with a visible left ventricular cavity, slices with merely a small muscle cap were excluded. New points are interpolated where the planes intersect the lines. This yields a set of corresponding boundary points for each sampled left ventricle across the population of ventricles (Figure 7.4).

7.3.3 Three-Dimensional Point Distribution Models

Aligning shape samples to a common scale, rotation, and translation is important for a compact model to be generated during the PCA stage. Procrustes

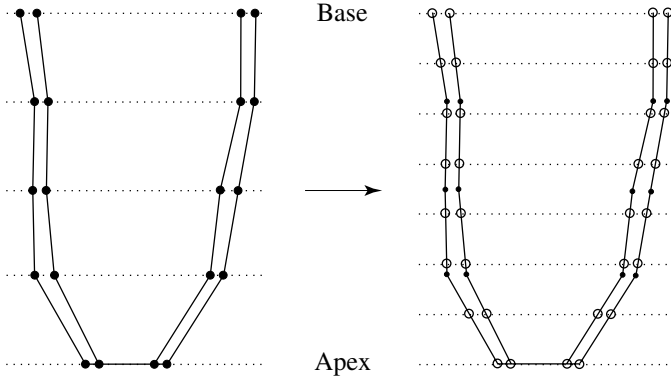


Figure 7.4. A cross-sectional depiction of transforming a cardiac MR stack with manually placed landmarks to a normalized cylindrical coordinate system.

analysis [50, 51] is used whereby an arbitrary shape is selected as the initial average shape estimate. All the other shapes are aligned to this average using a least-squares minimization. A new average is computed by a simple mean across the corresponding points, and the algorithm repeats until convergence.

For the 2D case, aligning one shape to another can be solved analytically by minimizing scale, rotation, and translation terms. Extending to 3D, the minimization of scaling, translations, and rotation differences along the three axes may lead to singularities known as gimbal lock. Assuming that 3D translation is represented by a separate translation vector \mathbf{t} , a quaternion \mathbf{q} representation of scaling and rotation avoids such behavior [52].

A quaternion \mathbf{q} is defined as the linear combination of a scalar term $q_0 \geq 0$, and three right-handed orthonormal vectors (\mathbf{i} , \mathbf{j} , and \mathbf{k}) :

$$\mathbf{q} = q_0 + q_1\mathbf{i} + q_2\mathbf{j} + q_3\mathbf{k}. \quad (7.3)$$

Together, the position and orientation of a 3D object can be represented as a seven-element pose vector $(\mathbf{q}|t) = [q_0, q_1, q_2, q_3, t_i, t_j, t_k]$.

The alignment of two 3D shape instances is accomplished using a well-known procedure given by Besl and McKay [53] to optimize for \mathbf{q} and \mathbf{t} . Aligning all the shapes is a matter of employing the Procrustes analysis using Besl's procedure to calculate the pose parameters. Once shape alignment is finished, principal component analysis is applied to the 3D models in a way that is no different from the conventional 2D application [35].

7.3.4 Modeling Volume Appearance

The first part of creating an appearance model of volume is to warp all the sample volumes to the average shape to eliminate shape variation and bring

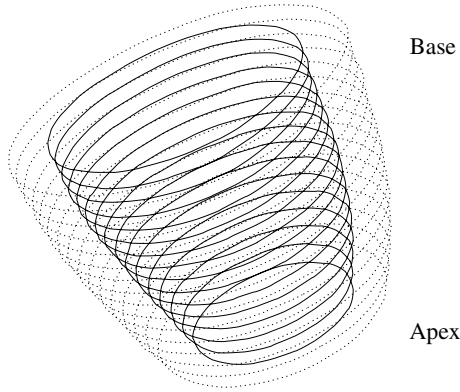


Figure 7.5. A wireframe representation of the mean LV shape in the normalized cylindrical coordinate system.

voxelwise correspondence across all the training samples, such that the voxel intensities can be represented as a shape-free vector of intensity values. Warping an image \mathbf{I} to a new image \mathbf{I}' involves creating a function which maps control points \mathbf{x}_i to \mathbf{x}'_i as well as the intermediate points in between. For the 2D case, either piecewise affine warping or thin-plate spline warping is adequate. In our models piecewise warping is preferred because it is significantly faster than thin-plate spline warping.

In 2D piecewise affine warping, landmark points are used to construct the shape area as a set of triangles. The well-known Delaunay triangulation algorithm is suitable for computing such a triangular mesh and can be found in many computational geometry references. Individual triangular patches are locally warped using barycentric coordinates. Given a triangle with the three corners, \mathbf{x}_1 , \mathbf{x}_2 , and \mathbf{x}_3 , we can represent any point \mathbf{x} within the triangle as $\mathbf{x} = \alpha\mathbf{x}_1 + \beta\mathbf{x}_2 + \gamma\mathbf{x}_3$ where $\gamma = 1 - (\alpha + \beta)$ and $\alpha + \beta + \gamma = 1$. In order for a point \mathbf{x} to fall inside a triangle, $0 \leq \alpha, \beta, \gamma \leq 1$ must be true.

Piecewise affine warping is implemented as follows:

- For each pixel location \mathbf{x}' in \mathbf{I}' :
 - Find the triangle t' which contains \mathbf{x}' by solving α , β , and γ for each triangle and finding the triangle where $0 \leq \alpha, \beta, \gamma \leq 1$.
 - Find the equivalent pixel location \mathbf{x} by computing $\mathbf{x} = \alpha\mathbf{x}_1 + \beta\mathbf{x}_2 + \gamma\mathbf{x}_3$ where \mathbf{x}_1 , \mathbf{x}_2 , and \mathbf{x}_3 are the triangle points from the original image.
 - Copy the pixel value in \mathbf{I} located by \mathbf{x} into the warped image \mathbf{I}' located at \mathbf{x}' . Some form of pixel interpolation such as bilinear may be used at this stage.

In our 3D models, piecewise affine warping is extended to tetrahedrons with four corners, \mathbf{x}_1 , \mathbf{x}_2 , \mathbf{x}_3 , and \mathbf{x}_4 . Any point within the tetrahedron is represented as $\mathbf{x} = \alpha\mathbf{x}_1 + \beta\mathbf{x}_2 + \gamma\mathbf{x}_3 + \delta\mathbf{x}_4$. In a general case, creating a tetrahedral representation of volume is solved using a 3D Delaunay triangulation

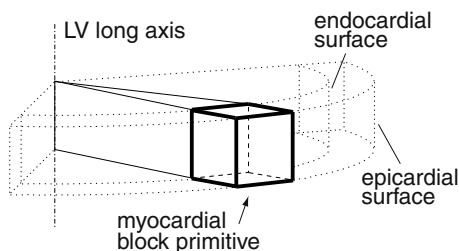


Figure 7.6. Definition of myocardial block primitives from concentric wedges.

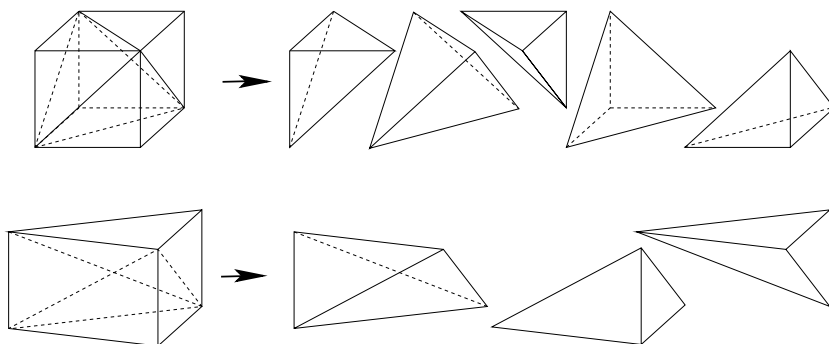


Figure 7.7. Decomposition of a cube (above) and a wedge (below) into tetrahedrons.

algorithm. However due to the cylindrical nature of the LV shape, a manually defined volume partitioning in regular tetrahedrons was utilized. Each slice level is constructed of pie-shaped wedges built on three tetrahedrons with exterior profile cubes built with five tetrahedrons (Figures 7.6, 7.7). Piecewise affine warping is implemented in a similar fashion as the 2D case. Because all volumes are warped to the average volume, barycentric coordinates, $\alpha, \beta, \gamma, \delta$ are precomputed for each fixed voxel point eliminating the time-consuming process of searching for the enclosing tetrahedron for each voxel point during the matching. Due to the regular geometry of the tetrahedrons in our volume partitioning, the barycentric coordinate computation did not become ill posed.

After the warping phase, the shape-free intensity vectors are normalized to an average intensity of zero and an average variance of one to remove the effects of brightness and contrast variations across scans. Next, PCA is applied to the shape-free intensity vectors to create an intensity model. In agreement with the AAM principle, shape information and intensity information are combined into a single active appearance model. Lastly, another PCA is applied to the coefficients of the shape and intensity models to form a combined appearance model [54].

In the equations below, the subscript s corresponds to shape parameters while the subscript g represents intensity (gray-level) parameters. To summarize, the 3D AAM is created as follows:

1. Let \mathbf{x}_i denote a vector of 3D landmark points for a given sample i . Compute a 3D PDM and approximate each shape sample as a linear combination of eigenvectors, where $\mathbf{b}_s = P_s^T(\mathbf{x} - \bar{\mathbf{x}})$ represents the sample shape parameters.
2. Warp each image to the mean shape using a warping such as piecewise affine or thin plate spline warping to create shape-free intensity vectors.
3. Normalize each intensity vector, applying a global intensity transform with parameters \mathbf{h}_i , to match the average intensity vector $\bar{\mathbf{g}}$.
4. Perform a PCA on the normalized intensity images.
5. Express each intensity sample as a linear combination of eigenvectors, where $\mathbf{b}_g = P_g^T(\mathbf{g} - \bar{\mathbf{g}})$ represents the sample shape parameters.
6. Concatenate the shape vectors \mathbf{b}_s and gray-level intensity vectors \mathbf{b}_g in the following manner

$$\mathbf{b} = \begin{pmatrix} W\mathbf{b}_s \\ \mathbf{b}_g \end{pmatrix} = \begin{pmatrix} WP_s^T(\mathbf{x} - \bar{\mathbf{x}}) \\ P_g^T(\mathbf{g} - \bar{\mathbf{g}}) \end{pmatrix}, \quad (7.4)$$

the weighting matrix W is a diagonal matrix relating the different units of shape and intensity coefficients.

7. Apply a PCA to the sample set of all \mathbf{b} vectors, yielding the appearance model

$$\mathbf{b} = Q\mathbf{c}. \quad (7.5)$$

7.3.5 Active Appearance Models: 3D Matching

Matching an appearance model to image data involves minimizing the root-mean-square intensity difference between the image data and appearance model instance by modifying the affine transformation, global intensity parameters, and the appearance coefficients. A gradient descent method is used that employs the relation between model coefficient changes and changes in the voxel intensity difference between the target image and synthesized model [54]. This relation is derived during a training stage.

Let \mathbf{t} and \mathbf{q} represent the translation and quaternion transformation parameters, and \mathbf{h} the intensity transform parameters. As shown above, shape \mathbf{x} is derived in the target image from the appearance coefficient \mathbf{c} and the affine transformation vectors \mathbf{t} and \mathbf{q} . Then, shape intensity vector \mathbf{g}_s is sampled from the target volume data after warping the space defined by \mathbf{x} to the mean shape \bar{x} . The model intensity vector \mathbf{g}_m is derived from the appearance coefficients \mathbf{c} with the global intensity corrected via \mathbf{h} . The error function, E , is the root-mean-square difference of $\mathbf{g}_s - \mathbf{g}_m$.

Gradient descent optimization requires the partial derivatives of the error function defined by the intensity of the target and synthesized model volume. While it is not possible to create such a function analytically, these derivatives may be approximated using fixed matrices computed by randomly perturbing model coefficients for a set of known training images and observing the resulting difference in error images [54]. Using a set of training images, their corresponding modeling parameters \mathbf{c} , \mathbf{t} , \mathbf{q} , and \mathbf{h} are randomly displaced, thus creating a difference between \mathbf{g}_s and \mathbf{g}_m . From the parameter displacements and the resulting difference intensity vectors, gradient approximating matrices A_c , A_t , A_q , and A_h can be determined using reduced-rank multivariate linear regression. Alternatively, the gradient matrices may be built one column at a time by averaging the Gaussian weighted differences between the target and synthesized image of each individual model perturbation. The latter method is preferred for 3D AAM matching due to lower memory requirements, better representation of high-order eigenmodes, and faster computation. This iterative refinement technique of precomputed fixed matrices versus brute force gradient descent optimization was formulated by Cootes [43] as well as by Baker and Matthews [55]. Formally, the gradient matrices are created as follows:

1. Select an object from the training set with known appearance model parameters \mathbf{c}_0 , \mathbf{t}_0 , \mathbf{q}_0 , and \mathbf{h}_0 .
2. For each element in the model parameters, \mathbf{c} , \mathbf{t} , \mathbf{q} , or \mathbf{h} , perturb a single element by a fixed $\delta\mathbf{p}$ with the rest of $\delta\mathbf{c}$, $\delta\mathbf{t}$, $\delta\mathbf{q}$, and $\delta\mathbf{h}$ assigned to zero. Typically, \mathbf{c} is perturbed within ± 1.5 standard deviation, \mathbf{t} by 3-5 voxels, and \mathbf{q} , \mathbf{h} by 10% of their original value.
3. Let $\mathbf{c} = \delta\mathbf{c} + \mathbf{c}_0$. Compute shape \mathbf{x} and texture \mathbf{g}_m .
4. Apply an affine transformation to \mathbf{x} by first transforming \mathbf{x} using $\delta\mathbf{t}$ and $\delta\mathbf{q}$, then transforming the result by \mathbf{t}_0 and \mathbf{q}_0 . This cascaded transform is required to maintain linearity.
5. Create the image patch \mathbf{g}_s warped from the target image to the mean shape using shape \mathbf{x} .
6. Apply global intensity scaling to \mathbf{g}_s by using $\delta\mathbf{h}$ first and then scaling the result by \mathbf{h}_0 .
7. Compute $\delta\mathbf{g} = \mathbf{g}_s - \mathbf{g}_m$.
8. Compute the slope, $\delta\mathbf{s} = \delta\mathbf{g}/\delta\mathbf{p}$. Weight the slope by a normalized Gaussian function with the ± 3 standard deviation is set to the maximum and minimum model perturbation values.
9. Accumulate the slope with previous slopes for that given element.
10. Go to step (2) and repeat until all elements and perturbations of each element are sufficiently covered. Place the average slope into the appropriate column in the gradient matrices A_c , A_t , A_q , or A_h .
11. Go to step (1) and repeat until there is sufficient coverage of displacement vectors.

The corresponding model correction steps are computed as

$$\delta \mathbf{c} = A_c (\mathbf{g}_s - \mathbf{g}_m), \quad (7.6)$$

$$\delta \mathbf{t} = A_t (\mathbf{g}_s - \mathbf{g}_m), \quad (7.7)$$

$$\delta \mathbf{q} = A_q (\mathbf{g}_s - \mathbf{g}_m), \quad (7.8)$$

$$\delta \mathbf{h} = A_h (\mathbf{g}_s - \mathbf{g}_m). \quad (7.9)$$

Matching the AAM to the image data is accomplished as follows:

1. Place the mean appearance model ($\mathbf{c}, \mathbf{h} = 0$; \mathbf{t}, \mathbf{q} defined by the initial model position) roughly on the object of interest and compute the difference image $\mathbf{g}_s - \mathbf{g}_m$.
2. Compute the root-mean-square (RMS) error of the difference image, E .
3. Compute the model corrections $\delta \mathbf{c}$, $\delta \mathbf{t}$, $\delta \mathbf{q}$, and $\delta \mathbf{h}$ from the difference image [Equations (7.6)–(7.9)].
4. Set $k = 1$.
5. Compute new model parameters as $\mathbf{c} := \mathbf{c} - k\delta \mathbf{c}$, $\mathbf{t} := \mathbf{t} - k\delta \mathbf{t}$, $\mathbf{q} := \mathbf{q} - k\delta \mathbf{q}$, and $\mathbf{h} := \mathbf{h} - k\delta \mathbf{h}$.
6. Based on these new parameters, recompute $\mathbf{g}_s - \mathbf{g}_m$ and find the RMS error.
7. If the RMS error is less than E , accept these parameters and go to step (2).
8. Else try setting k to 1.5, 0.5, 0.25, 0.125, etc., and go to step (5). Repeat steps (5)–(8) until the error cannot be reduced any further.

7.3.6 Case Study

To investigate the clinical potential of the 3D active appearance model under clinically realistic conditions, AAM's were trained and tested in multislice short-axis cardiac magnetic resonance images collected from 38 normal subjects and 18 patients yielding a total of 56 short-axis 3D cardiac MR data sets. Patients were selected suffering from different common cardiac pathologies (amongst others, different types of myocardial infarction, hypertrophic cardiomyopathy, arrhythmia). Images were acquired using standard ECG gated fast field echo MR pulse sequences on a Philips Gyroscan NT 15 scanner. Slices were acquired in a per-slice manner, under breathhold in end-expiration. End-diastolic images were used in this study. Image resolution was 256×256 pixels, with a field of view of 400–450 mm, slice thickness 8–11 mm. Between 8 and 14 slices were scanned to at least cover the entire left ventricle, depending on LV dimensions and slice spacing.

In midventricular short-axis MR images, the left ventricle can usually be identified as an approximately circular object (Figure 7.8a). This fact is used for automated initialization of the 3D AAM. A previously validated Hough transform based method determines a 2D centroid of the LV long axis for each MR image slice [56]. A 3D centroid of a line segment fitted through the 2D centroids of individual MR slices defines the initial position of the 3D AAM.

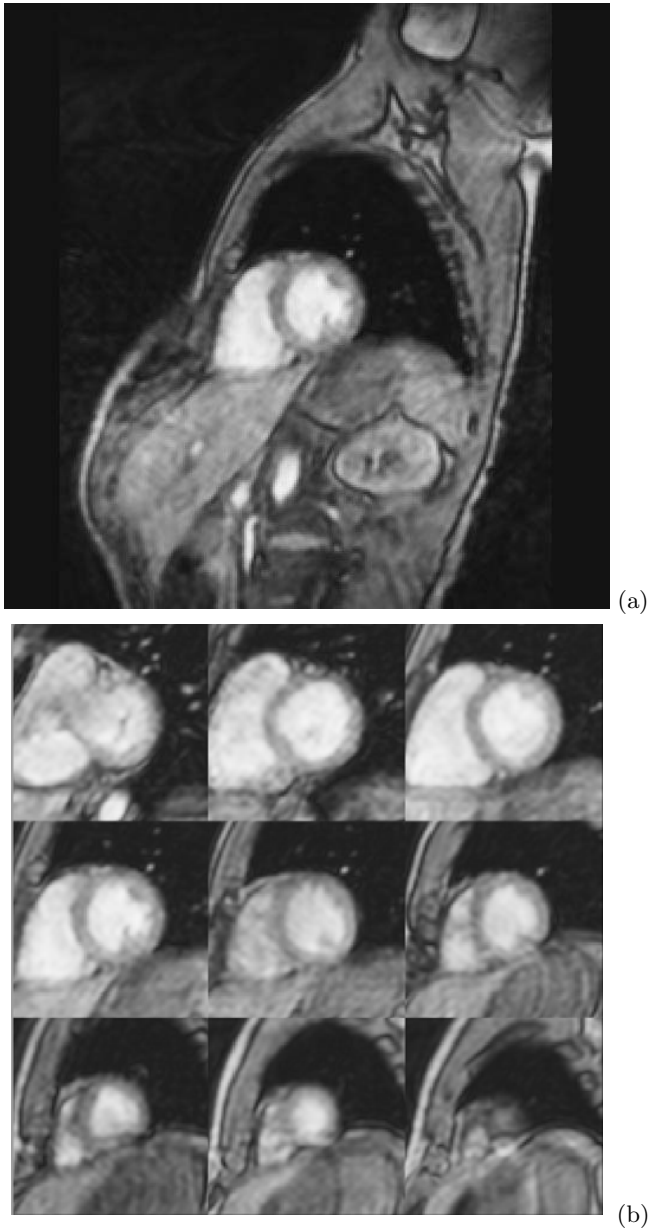


Figure 7.8. Example cardiac MR images used for validation. (a) Left-ventricular segmentation was performed in volumetric images consisting of 8–12 full-size MR images like the one shown here. (b) Subimages depicting LV detail in all 9 images of this volumetric data set. See Plate I for the segmentation results.

To make the 3D segmentation procedure completely independent from any user interaction regarding the rotation and scale of the heart in the short-axis plane, the matching process was repeatedly performed for a range of five orientations and three scales. This multiple initialization is important because AAM matching may be dependent on initial positioning since gradient descent may contain local minima. The matching result yielding the smallest quadratic intensity error was selected as the final match. The matching procedure resulted in a set of endo- and epicardial contours for each volumetric MR image.

Left ventricular endocardium and epicardium were manually traced by an expert observer who was blinded to the results of the computer analysis, these borders defined the independent standard. To quantitatively assess the performance of the 3D AAM approach, surface positioning errors were determined comparing the automatically detected endo- and epicardial surfaces with the independent standard. The average signed and unsigned surface positioning errors were defined by measuring the distances between points along rays perpendicular to the centerline between the respective manual contours and the computer-determined surfaces; 100 rays were used for each contour. Surface positioning errors are expressed in millimeters as mean \pm standard deviation. Negative sign of the signed error value means that the automatically-determined surface was inside of the observer-defined surface.

Three clinically important measures were calculated and used for performance assessment: LV cavity volume, LV epicardial volume, and LV myocardial mass. The volumetric indices were determined using all slices for which both manually traced contours and computer-determined surfaces were available and were expressed in cm^3 . The LV mass measurements are reported in *g*. Regression analysis was used to compare the computer measurements with the independent standard.

Plate I shows an example of an automatically analyzed volumetric MR data set. PLATES II demonstrates several stages of the model matching process, starting with the initial model position and ending with the final fit. Mean signed endo- and epicardial surface positioning errors were -0.46 ± 1.33 mm and -0.29 ± 1.16 mm, respectively, showing a slightly negative border detection bias. The mean unsigned positioning errors were 2.75 ± 0.86 mm for the endocardial contours and 2.63 ± 0.76 mm, for the epicardium, demonstrating small absolute differences from the independent standard (voxel sizes ranged from $1.56 \times 1.56 \times 8$ mm to $1.76 \times 1.76 \times 11$ mm). A very good correlation of the manually-identified and 3D AAM-determined LV endo- and epicardial volumes as well as correlation of computer-determined LV wall mass with the independent standard were achieved – ($y = 0.88x + 8.4, R^2 = 0.94$; $y = 0.91x + 12.1, R^2 = 0.97$; $y = 0.80x + 17.9, R^2 = 0.82$, respectively).

7.3.7 Extension to 4D Analysis

The heart is a dynamic system making time-independent segmentation inadequate. Applying 3D AAM segmentation to the full cardiac cycle would require multiple models for different phases because any temporal knowledge of the interrelationship between frames would be lost. Several existing methods have been developed for 3D + time cardiac segmentation taking into account the temporal relationship between frames. For example, one technique by Jacob et al. [57] solves temporal coherency between active shape models in echocardiograms through the use of a Kalman filter creating a motion model to predict the cardiac cycle in addition to a shape model. An alternative method by Montagnat *et al.* [58] segments cylindrical echocardiographic images using deformable models. Here temporal coherence is accomplished by reinitializing the deformable model using the previous segmentation, while incorporating a 4D anisotropic diffusion filter that significantly improves the spatial and temporal information between frames.

To extend the 3D AAM framework to 3D + time, we propose to incorporate a time element to the model by phase normalizing objects to a common time correspondence and concatenating shape and texture vectors of individual phases into a single shape and texture vector. Such a technique has been found efficient in 2D + time AAM and ASM models [47, 46, 59] and is promising as a future extension of 3D AAMs.

7.4 Vascular MR Image Analysis

7.4.1 Magnetic Resonance Angiography

Magnetic resonance angiography (MRA) is a powerful clinical tool that challenges the preeminence of conventional contrast angiography — the gold standard of vascular imaging. MRA offers combined imaging of vascular and soft tissues during a single comprehensive examination.

The automatic segmentation and labeling of the vascular structures are motivated by the clinical desire for quantitative information about a patient's vascular anatomy and function. Various cardiovascular problems, including aneurysms and stenoses, can be more accurately assessed using volumetric information than from x-ray angiographic projections. It is time consuming and impractical to manually segment the vessel structures to be analyzed. This indicates the need for robust and quick methods to perform accurate separation and identification of vascular structures within the anatomy with a minimal amount of user interaction. This segmentation can then be used to perform clinically useful tasks, including selective visualization (region of interest display), and quantitation of an individual's vascular function.

7.4.2 Methods for Vascular MR Segmentation

The volumetric segmentation techniques were preceded by numerous attempts to visualize vascular structures in 3D from 2D projections [60, 61, 62, 63, 64]. These approaches continue to be used in x-ray angiography. After the arrival of MR in sufficient speed and resolution, Fessler and Macovski developed a detailed object-based approach to the reconstruction of the arterial trees using projections from magnetic resonance angiograms [62]. Although they were using MR, which is inherently volumetric, they utilized concepts from earlier research and used planar images as the basis for their reconstruction technique. Garreau et al. further refined the mapping and biplane angiography reconstruction issues by introducing an expert knowledge base to give a map of the topology of the vessel paths [63]. This knowledge base was used as a basis for structure and feature labeling of the vessel tree.

More recent work in the area of vessel segmentation uses 3D MR or CT data sets. Clearly, similar analysis methodologies can be utilized for MRA and CTA (computed tomography angiography). Some of the less complex approaches involve direct segmentation of the data without modeling of the vessel structure or explicit determination of the vessel path. An example of such an approach can be found in [65] where abdominal aortic aneurysms are segmented and quantified directly from the image data. The user selects two starting points in the distal iliac arteries and the segmentation algorithm travels in a proximal direction along the center of the vessels, determining the lumen outline of iliac arteries and the abdominal aorta in CTA volumes. More comprehensive segmentation of the cerebral vessels in CTA and MRA has been accomplished using an iterative dilation approach [66]. A bounded space dilation operation was used to build up a vessel tree. Cerebral arteries were well segmented and the algorithm avoided inclusion of neighboring bone structures and thin connections to adjacent regions by additional restrictions on the growth process. This work is notable as a method which has the ability to indicate where bifurcations of the vessels occur, as the growth front algorithm can readily determine when a newly grown region is not connected in the 3D space. Bifurcation detection is a crucial portion of the overall vessel segmentation process, especially in algorithms that utilize topology analysis as an aid to segmentation.

In addition to direct 3D segmentation approaches, several preprocessing methodologies exist that are worth discussing, most notably finding central axes of the elongated vascular structures using 3D skeletonization [67, 68, 69] or by identifying vessel medial axes and cores [70]. A complete segmentation and analysis package for coronary angiograms was described by Higgins et al. [69] which used skeletonization to determine the central axes of vessel paths in 3D CTA data sets. Segmentation and quantitation of the coronary arteries were performed in an integrated system. The central paths determined by a 3D skeletonization algorithm were used as the guiding topological map for the segmentation.

Finding the central axes of vessels using a medial axis transform is another powerful approach. The concepts of height ridges and medial axes were extended to the concept of core atoms by Pizer *et al.* [71, 72, 70]. They extended the medial axis concept to gray-scale images and defined a quantifiable notion of medialness — the core. A core is a locus in a space whose coordinates are position, radius, and associated orientations [70]. Vessel central axes are characterized by high medialness, thus relating them to cores. Core transform finds the center of the vessel through a specific computation of the medial axis and follows the local maxima along the path of vessel propagation as a step in image segmentation. The concept of core atoms encapsulates information about edge direction, radius, and shape. Each core atom holds information about two edge elements and is located midway in between these two edge elements. Using statistical methods, the core atoms can indicate a vessel path or other anatomic shape [72]. Section 7.4.3 discusses this approach in more detail.

A codimension 2 geodesic active contour approach is under development by Lorigo *et al.* [73]. A mathematical modeling technique is used to represent complicated curvelike structures of vasculature as seen in 3D MRA image data. The segmentation task is defined as an energy minimization problem over all 3D curves. Mean curvature evolution techniques that were previously developed and implemented with level set methods [74, 75, 76] were extended to a higher codimension and applied to segmentation of brain vessel vasculature. While this approach needs to mature before it reaches clinical applicability, it represents an interesting and promising direction.

Despite the fact that most of the methods employed to segment vessels from 3D image data sets are very different in implementation, two main concepts are commonly utilized. The first concept is that of determining the center of the vessel paths. The following of a particular vessel path is the crucial step in understanding the vessel topology that is important for segmentation. The second concept is the use of some a priori knowledge about the segmentation task. This knowledge can be used to provide a road map to either guide the segmentation process or to identify structures with physically relevant names. It is the application of these two major concepts that form the basis for most of the recently developed methods that are outlined in the following discussion.

Separation of arteries and veins is an emerging challenge in MRA analysis. With the development of new MR contrast agents that have longer persistence in the blood, there is the ability to image the vasculature fully enhanced and at high resolution. These high-resolution “steady state” images have simultaneous enhancement of both the artery and vein blood pools (Figure 7.9). This enhancement can be useful. However, it can also obscure critical detail when analyzing the vessels using maximum intensity projection and other visualization strategies. Artery–vein separated images have unobstructed artery visualization comparable to dynamic MRA scans. Nevertheless, they do not suffer from the limited resolution that is necessary to achieve a dynamic im-



Figure 7.9. Maximum intensity projection of a typical blood-pool contrast enhanced MRA data set of the abdomen and lower extremities.

age sequence. To meet the incompatible goals of high resolution with the ability to view unobstructed arterial vessels, artery–vein separation and selective visualization techniques must be developed to achieve acceptance of contrast-enhanced MRA as an alternative to x-ray angiography. Currently, separation of arteries and veins in MRA images is limited to research applications and manual segmentations. Recently, there has been considerable progress and several different approaches have shown potential as a method for artery–vein separation.

Generally, artery–vein separation methods can be divided into two categories — acquisition based methods [77, 78, 79] and postprocessing techniques [62, 66, 67, 68, 69, 70]. Acquisition-based techniques seek to exploit various

flow and physical properties. Phase behavior and time series acquisitions image the vessels attempting to provide information about the vessel identity directly from the imaging protocol itself. Postprocessing techniques seek to provide the arterial-venous separations by analyzing the acquired data after the scan is performed. These methods have to rely on information present in the scan itself, while having the advantage of not being tied to a particular protocol or scan type. These methods vary in complexity and all of them employ user interaction to some extent. Another postprocessing approach seeks to segment the artery and vein using image intensity properties to determine a membership in an artery or vein. Two representative methods of this research are gray-scale connectivity [80] and fuzzy connectivity [81].

7.4.3 Vasculature Assessment via Tubular Object Extraction and Tree Growing

One of the prominent characterizations of vessel shape is undoubtedly their tubular character. As mentioned above, Pizer et al. developed a generalized methodology for determination of central axes of tubular structures via calculation of intensity ridges, medialness, and cores in gray level images [82, 70]. This concept was applied to time-of-flight MRA images by Aylward et al. [83] and further extended to a vascular tree representation by Bullitt et al. [84].

The main steps of the method are given in the following algorithm:

1. Vasculature assessment via tubular object extraction and tree growing.
2. Geometry-based semi-automated segmentation of the MRA volume to extract individual vessel segments in the region of interest.
3. Comparison of the extracted vessel segments with the maximum intensity projection of the original MRA data in the region of interest. If vessel segments are missing, repeat step (1).
4. Iterative construction of a vessel tree.
5. 3D visualization and interactive editing of the resulting vessel tree.

Extraction of each vessel segment starts from a user-supplied seed point. A vessel segment is a nonbranching 3D portion of the vasculature. Using the seed point, image intensity ridges are automatically extracted utilizing user-supplied information about the approximate width of the segmented vessel. As a result, the medial axis (skeleton) of the vessel segment is formed. The vessel segment's width is determined at each point of the skeleton under the assumption that the vessel is approximately circular. The width is calculated to be proportional to the scale that produces maximal response from a cylindrical medialness measure. The vessel segmentation process is repeated for all vessel segments in the region of interest, yielding a set of unbranched, directed 3D skeleton curves with a width associated with each point [83].

The segmentation step is complete when the maximum intensity projection of the original MRA data agrees with the visualization of the vessel segments resulting from the segmentation. If vessel segments are missing in the region

of interest, the segmentation process is continued from newly identified seed points.

Before the vasculature tree is constructed, several potential problems of the identified vessel segments must be considered since the result of vessel extraction may not be ideal:

- Spurious vessel segments must be eliminated.
- Excessively long vessel segments extending past one or more branches must be divided.
- Adjacent vessel skeletons belonging to the same vessel must be connected.
- Directionality of blood flow must be determined.

All these problems are addressed during the tree construction step.

The tree construction process utilizes linear distance properties of individual vessel segment skeletons and the image intensity of the original MRA data. During the segment-connecting process, I and Y connections are allowed while X connections are not. Consequently, at least one end-point of the two segments to be connected is engaged. Tree construction starts from one or more interactively identified tree roots. The maximum distance to be considered for establishing a connection between two segments is specified by the user. Starting with the root nodes, a tree is constructed by iterative addition of segments that satisfy both the distance and intensity criteria.

The sequence of forming tree segment connections is controlled by the *connection cost* CC with the best possible connection being realized at each iteration. For each two segments, one is considered a potential parent (the one already connected to the tree root) and one is a potential child. Three pairs of possible connections are determined and a line is constructed connecting each pair of points in the 3D image. These lines form three axes along which hollow cylinders are constructed with radii slightly greater than that of the potential child segment so that the cylinder surface is positioned outside of the child vessel. The *intensity ratio* is defined as a ratio of the average image intensities of a cylinder surface and its axis. A low ratio (bright central axis and dark cylinder surface) is considered to be evidence of a valid connection. The connection cost is defined as a weighted sum of the *linear distance* LD of the connected segments and the intensity ratio IR :

$$CC = LD + 4 IR . \quad (7.10)$$

The connection of a minimum cost CC is identified and formed. After the best connection from all possible ones is found, flow direction in the connected segment may be reversed to agree with that of the already formed tree. The spurious segments mentioned earlier are to a large extent removed automatically since they fail to meet the connectivity requirements of distance and intensity.

As can be expected, the process described above may lead to missing or incorrect connections caused by MR imaging artifacts, a limited size of the

imaged region of interest, or other ambiguities present in MR data. Therefore, the resulting tree is carefully inspected and editing tools are employed to include missing connections and remove inappropriate ones. The user is allowed to delete proximal or distal segments and associated subtrees, delete an entire vessel and the associated subtree, disconnect a subtree from a parent and reconnect it to another user-specified parent or parent point, and reverse blood flow in any segment (causing automated update of the parent-child data structure).

7.4.4 Knowledge-Based Approach to Vessel Detection and Artery–Vessel Separation

The following algorithm was developed to perform arteriovenous separation in the peripheral vasculature, specifically the iliac and femoral vessels. When analyzing intravascular contrast agent-enhanced MRA data sets that image this area, the most challenging aspect to overcome is the partial volume effects brought on by limited spatial resolution and the proximity of the vessels. These effects cause the artery and vein segments to become aliased within some voxels of the data, causing incorrect connections between the artery and vein pathways, when in reality there is only close proximity between the two. These incorrect connections cause simpler methodologies such as region growing to fail in separating the arteries and veins into two distinct objects.

To cope with this problem, a knowledge-based method was developed and tested by Stefancik and Sonka that consists of the following main steps [85], Figure 7.10.

1. Knowledge-based segmentation of arterial and venous trees in lower extremities
2. Binary mask generation — the contrast-enhanced MRA data are segmented in a 3D connected combined vessel tree (consisting of arteries and veins) and nonvessel regions.
3. Tree-structure generation — the combined vessel tree is topologically described as a tree structure using vessel-bounded space dilation for identification of bifurcations.
4. Optimal vessel path calculation — vascular central axes are determined using 3D dynamic programming in a vessel-bounded space.
5. Vessel segment labeling — vessel segments are labeled as belonging to arteries or veins.
6. Conflict resolution — if any branch segment belongs to more than one path through the tree, individual voxels within that segment are assigned to their appropriate paths and their anatomic labels.

These main steps will now be described in more detail.

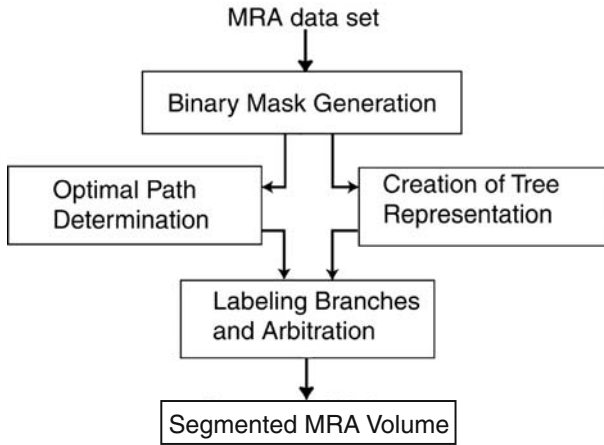


Figure 7.10. Graphical overview of the segmentation process described in the text.

Binary Mask Generation

The combined vessel tree consisting of arteries and veins and forming a binary volumetric mask is acquired by a two-step process — percentage-based gray-scale threshold calculation is followed by a seeded region growing. For the abdominal region and lower extremities, the vessel structures occupy approximately 5% of the data set by volume. Therefore, 95% thresholding is employed with a threshold value derived from a gray-level histogram [86]. As a result, virtually all vessels, some MRI artifacts, and some subcutaneous fat regions are segmented. To remove the imaging artifacts and subcutaneous fat from the binary mask, a seeded region growing operation follows. A seed point is identified within a vessel structure, and all connected voxels over the threshold value are labeled. All nonconnected voxels are then discarded. An example of the resulting combined tree is shown in Figure 7.13(a).

Tree-Structure Generation

For a vascular structure, it is reasonable to segment the vessel volume into vessel segments, with each segment representing a section between two subsequent bifurcations. The vessel segments forming a vessel tree serve as an aid to topology analysis and as a method of grouping voxels in structural primitives for subsequent processing.

The conditional bounded-space dilation operation of mathematical morphology [86] is used in the growth front algorithm tree generation [66]. The tree contains relevant information about continuous branch segments, and higher-level parameters such as length and volume can be calculated from these segments (Figure 7.11).

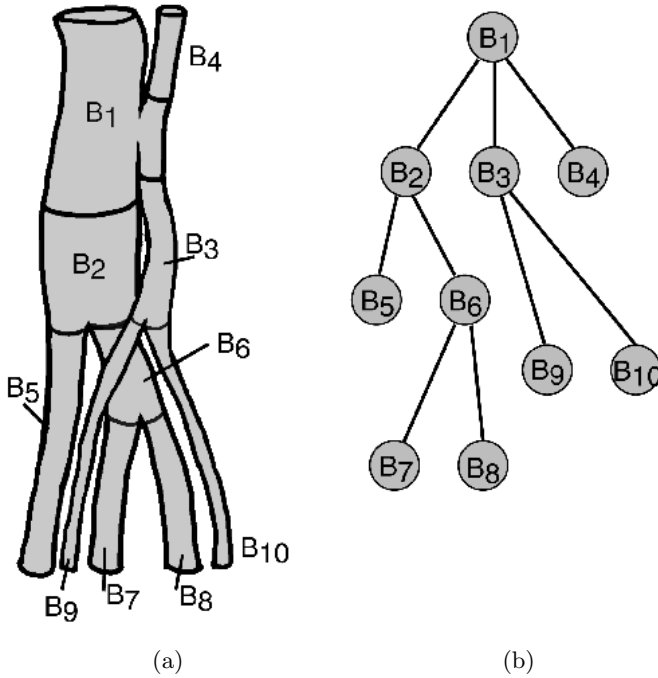


Figure 7.11. Tree structure representation. (a) Vessel tree with labeled branch segments. (b) Node topology created by the bounded-space dilatation growth algorithm.

Optimal Vessel Path Calculation

The complex topology of the combined tree along with multiple false bifurcations that are always present lead to an over-segmented tree which is not practical to label directly. Additional information about the spatial path of individual vessel segments is needed. The optimal vessel path is determined using a dynamic programming path cost maximization applied to 3D cost volumes corresponding to the analyzed 3D data set.

Vessel Segment Labeling

The optimal path calculation yields discrete paths through the volume that tend to follow the center of the vessel. Since the artery or vein label is known for each proximal seed point used for dynamic programming path search, this label is propagated to all vessel segments along the identified paths. When this labeling is performed for each path, segments may have conflicting labels — some of the segments are labeled as belonging to both arteries and veins. Such cases are solved by the conflict resolution step.

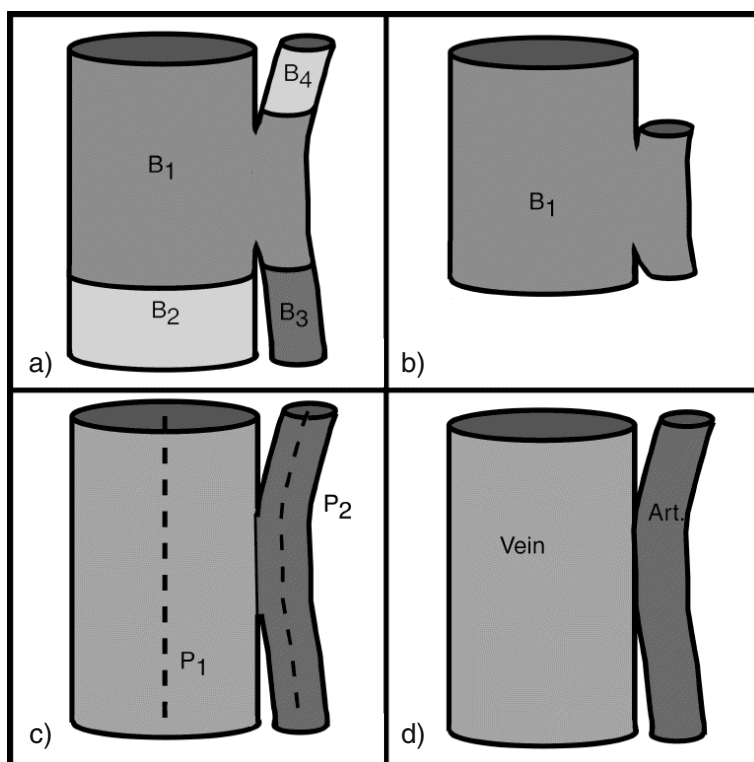


Figure 7.12. Conflict resolution: (a) Example area of combined artery and vein membership in one branch (B_1). (b) Branch B_1 is labeled as a contention branch. (c) Optimal paths and their radii of influence dictate voxel membership. (d) Artery and vein segmented.

Conflict Resolution

When a vessel segment has conflicting labels, a spatial decision conflict resolution function is invoked to resolve the labeling conflict. The employed decision function allows a specific vessel segment to label its voxels by different labels according to their proximity to the conflicting paths that run through that vessel segment (Figure 7.12). This effectively separates the artery and vein connections that occur due to the partial volume effects.

The algorithm presented above was tested in artificially generated data sets and in in vivo acquired MRA volumes that were acquired 5 minutes

post-injection of a blood pool contrast agent² [87]. The original image data are shown in Figure 7.9. Automatically and manually segmented data were compared to assess the performance of the automated method in separation of main vessels in the abdominal and upper leg area. The artery–vein labeling error ranged from 1 to 15%. Complete quantitative validation results can be found in [87]. Figures 7.13(a)–(b) show representative segmentation of two different data sets. Figures 7.13(c)–(d) show selective visualization of the segmented structures from Figure 7.13(b). As indicated above, this approach focused on the separation part and may benefit from improving the initial binary tree segmentation. The first step of the fuzzy connectivity approach described in the next paragraphs seems to be especially attractive for that purpose.

7.4.5 Fuzzy Connectivity Approach to Vessel Detection and Artery–Vessel Separation

Udupa et al. developed a fuzzy connectivity–based methodology for vessel extraction and artery–vein separation. The method is based on a principle of fuzzy connected image segmentation that was applied, e.g., to MR brain segmentation, multiple sclerosis lesion detection in MR data sets, and separation of bone and soft tissues from skin in CT images [88, 89]. This concept was further enriched by the recent addition of scale-based fuzzy connectivity [90].

The basic principle of this approach is the notion that image intensity information itself is insufficient for segmenting heterogeneous objects with varying image intensities within the objects. Variations of intensities may be caused by a plethora of reasons — imaging artifacts, noise, inhomogeneity of the object itself, etc. All these causes are common in medical images. Udupa et al. stated an important concept that voxels belonging to the same objects tend to hang together, thus defining objects by a combination of spatial relationship of their elements (pixels, voxels), at the same time considering the local image intensity properties. The spatial relationships should be determined for *each* pair of image elements in the entire image. To accomplish that, local and global image properties are considered.

The local fuzzy relation is called affinity and represents a strength of hanging togetherness of nearby image elements and has a value in $[0,1]$. The affinity is a function of the spatial distance between the two nearby image elements as well as of their image intensities or other intensity-derived features (e.g., edges). Fuzzy connectedness is then a global fuzzy relation that assigns every pair of image elements E_1 and E_2 a value in $[0,1]$ based on the hanging-togetherness values along all possible paths between these two image elements. Note that the elements E_1 and E_2 are not expected to be nearby. For each path, its strength is defined as the minimum affinity value for all pairwise elements of the path. In other words, the strength of the entire path is defined by the strength of its weakest local connection. Then, the value of fuzzy

² AngioMARK, EPIX Medical, Cambridge MA.

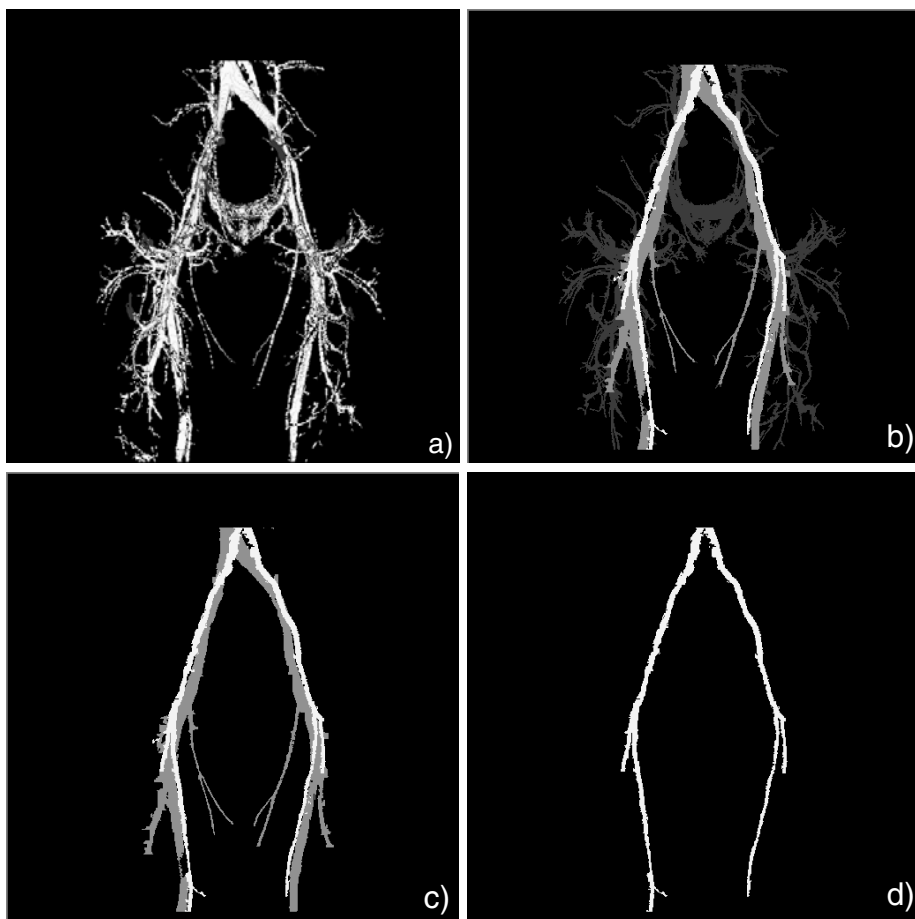


Figure 7.13. Segmentation of main arteries and veins in an MRA data set of abdomen and lower extremities. See Fig. 7.9 for maximum intensity projection of this data set. (a) Combined tree (volume rendering). (b) Main arteries and veins. (c) Selective visualization of major arteries and veins from (b). (d) Segmented arterial tree from (b).

connectedness (global hanging togetherness) of E_1 and E_2 is determined as the maximum of the strengths of all possible paths between E_1 and E_2 . The strength of connectedness of all possible pairs of elements defining a fuzzy connected object is determined via dynamic programming.

An approach for arterial and venous tree segmentation and artery-vein separation was developed based on fuzzy connectivity principles [81] and applied to blood-pool contrast enhanced images³ of abdomen and lower extremi-

³ AngioMARK, EPIX Medical, Cambridge MA.



Figure 7.14. Maximum intensity projection image of the original data used in Plate III. Courtesy of J. K. Udupa, University of Pennsylvania.

ties. First, an entire vessel tree is segmented from the MRA data sets utilizing absolute fuzzy connectedness. Next, arteries and veins are separated using relative fuzzy connectedness. For the artery–vein separation step, seed image elements are interactively determined inside an artery and inside a vein. Large-aspect arteries and veins are separated, smaller-aspect separation is performed in the following iterations, four iterations being typically sufficient. To separate the arteries and veins, a distance transform image is formed from the binary image of the entire vessel structure. Separate centerlines of arterial and venous segments between two bifurcations are determined using a cost function reflecting the distance transform values. All image elements belonging to the arterial or venous centerlines are then considered new seed elements for the fuzzy connectivity criterion, thus allowing artery–vein separation.

The vessel tree segmentation and artery–vein separation procedure is quite fast, requiring only several minutes to complete. Figure 7.14 and Plate III show the functionality of the method.

7.5 MR Assessment of Atherosclerotic Plaque

7.5.1 Vessel Wall Imaging

Recent studies indicate that the composition of atherosclerotic plaque lesions may be more important than the morphology. The depiction of the vessel lumen generated by most angiography techniques will be insufficient to determine the significance of lesions, such as whether they are stable or are likely to rupture.

Magnetic resonance imaging is capable of distinguishing between the different components of atherosclerotic plaque, identifying its composition in addition to its morphology and potentially providing a more clinically relevant assessment of the severity of disease. Direct imaging of the vessel wall depicts components of atherosclerotic plaque. Calcium, lipids, thrombus, and fibrous tissues each have distinct relaxation characteristics that can be measured by MRI using a multicontrast approach for tissue characterization.

Imaging of the vessel wall for plaque characterization is considerably more difficult than vessel lumen imaging. Signal generated by the vessel wall limits the signal-to-noise ratio that can be achieved, while the needed high resolution further reduces the available SNR. Comprehensive tissue characterization requires multiple image acquisitions to generate enough contrast weightings to distinguish between the major plaque components. In addition, blood signal must be thoroughly suppressed to achieve adequate contrast. This may be especially difficult in areas prone to slow or turbulent flow (such as the carotid bifurcation) where this signal may mimic that of a legitimate plaque lesion. Despite these obstacles, considerable progress has been made in finding feasible imaging protocols for imaging vessel wall in the aorta, carotid, and coronary arteries.

The most successful protocols to date in all three of these locations incorporate fast spin echo imaging coupled with cardiac gating (and respiratory gating in the case of the coronary arteries) and double inversion recovery (double IR) for blood suppression. The double IR preparation applies a non-selective inversion to the entire volume, followed by a second selective inversion to restore the magnetization in the imaged slice or slab. After waiting an appropriate time interval for blood signal to be nulled, a standard FSE sequence is applied to depict vessel wall and any associated plaque. This protocol may be used with either 2D multislice acquisitions or true 3D volumes. By acquiring T1-, T2-, and proton-density-weighted images, the major components of atherosclerotic plaque (lipid, calcification, fibrous cap) can be segmented. Two-dimensional acquisitions have been shown with resolution down to 0.4×0.4 mm in-plane with 2 mm slices, while true 3D acquisitions can reduce slice thickness to 0.5 mm. The need for high-quality blood suppression in the double IR sequence results in rather long acquisition times, and in the case of coronary imaging, respiratory motion suppression is necessary as well.

Several ongoing developments in atherosclerotic plaque imaging with MRI promise to further improve its capabilities. Imaging at higher field strengths

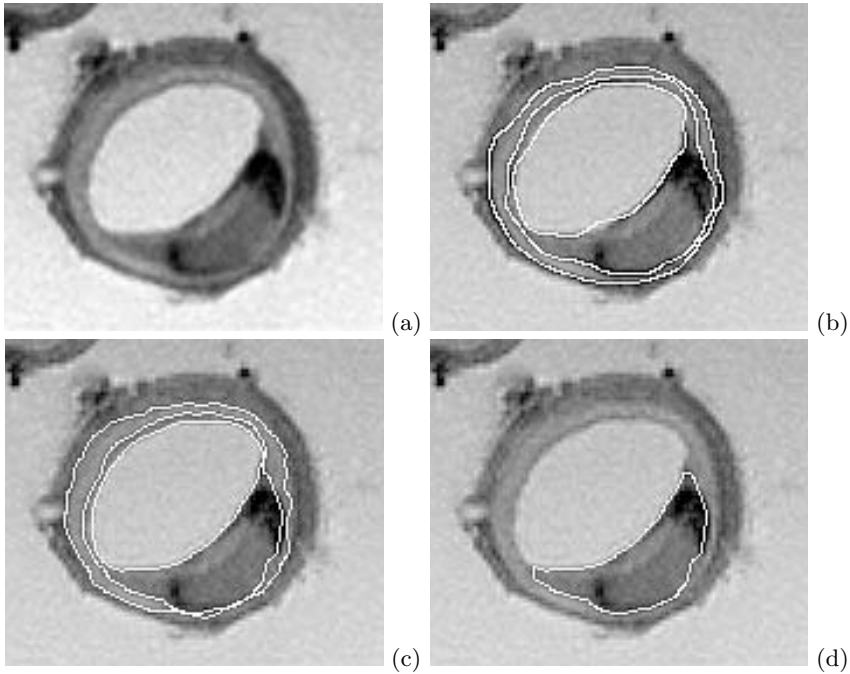


Figure 7.15. Example of segmented T2-weighted MR cross-section. (a) Original in vitro MR image of an excised artery, (b) observer-defined segmentation of lumen, intima-media, and adventitia-media borders, (c) fully automated segmentation, (d) identified region of plaque. MR image data courtesy of Drs. Stollberger and Holzapfel, Karl-Franzens University of Graz and Graz University of Technology, Austria.

(3T and beyond) will help improve SNR as such systems proliferate [91, 92]. Development of specialized receiver coils (including intravascular coils) may also dramatically improve image quality and resolution potential [93]. Contrast agents that are selectively absorbed by plaque components are also showing promise for plaque characterization [94, 95, 96, 93, 97, 98, 99, 100, 101, 102, 103].

7.5.2 Plaque Assessment via MR Wall Imaging

To determine plaque properties, MR images must have sufficient resolution to allow segmentation of the vessel wall. The segmentation results in determination of the morphology of the vessel wall and plaque. After that, plaque composition must be determined. This overall approach requires performing a sequence of complex steps [104].

Quantification of plaque morphology in high-resolution volumetric multi-contrast data (Plate IV) requires automated segmentation. To perform this

task, a previously developed and successfully method for automated design of border detection criteria [105] was employed that substantially simplifies implementation of new border-based image segmentation applications. All information necessary to perform image segmentation is automatically derived from a training set that is presented in the form of expert-traced segmentation examples. Therefore, borders of lumen, internal elastic lamina (intima–media), and external elastic lamina (media–adventitia) were manually traced in a set of training images. From these examples, border detection criteria using edge- and gray-level pattern information [105] were derived and used for segmentation of a testing set of images. Border detection errors were assessed in the testing set.

Five atherosclerotic iliac arterial segments were imaged in vitro as described above. The arterial wall layers and plaque were clearly visible as is shown in Plate IV. The corresponding histology demonstrated good agreement with the MR images. An example of an MR image Figure 7.15 (a) with automatically identified lumen, intima–media, and media–adventitia borders is shown in Figure 7.15 (b) (c). After training as described above, the borders automatically detected in a disjoint testing set were quantitatively compared with a manually-identified independent standard. The automated method yielded promising accuracy and minimal bias: root-mean-square and signed mean border positioning errors of the media–adventitia border detection were 1.03 ± 0.28 and 0.36 ± 0.35 pixel, respectively. Corresponding border positioning errors were 0.96 ± 0.12 and 0.34 ± 0.31 pixel for the intima–media borders and 1.04 ± 0.27 and 0.08 ± 0.45 pixel for the lumen border detection. Regions of plaque were identified as any portion of arterial wall with thickening between lumen–intima and media–adventitia borders (Fig. 7.15 d). This thickness can be determined directly from the boundaries (surfaces) identified in the volumetric MR images — an increased thickness indicates presence of plaque.

The achieved quality of MR images and the segmentation results are encouraging and facilitate further development of plaque vulnerability indices based on plaque mechanics [106]. Once noninvasive assessment of plaque vulnerability becomes available, the way in which atherosclerotic disease is diagnosed, monitored, and treated may change dramatically. Determination of plaque composition and its mechanical stress consequences will allow assessment of cardiovascular risks on a per-subject basis.

7.6 Conclusions

Computer vision methods are being employed in medical image analysis more and more frequently. MR imaging provides enormous flexibility to probe living bodies and deliver image information about the morphology, structure, and function of individual organs and their parts. Magnetic resonance imaging

and analysis of MRT images are indeed extremely powerful examples of how image processing techniques can be applied beyond the visible spectrum.

The chapter focused on describing basic principles of MR imaging and described several application areas in which automated image analysis will play a major role in the near future — segmentation and analysis of cardiac MR images, vascular MR angiography, and MR images of atherosclerotic plaque. In all of the covered application areas, the imaging is performed three-dimensionally and the analysis is three-dimensional as well. Needless to say, the step from 2D to 3D is not an easy one and many new solutions must be found to perform truly 3D medical image analysis. MR imaging is capable to deliver four dimensional information as well (3D + time).

To summarize, the field of MR imaging and MR image analysis is an extremely exciting one. The information about living bodies is provided in real time, in 4D, with consequences almost beyond human imagination. The amounts of data generated exceed the visual analysis capabilities of the diagnostic radiologists and call for development of reliable, accurate, precise, and fast quantitative techniques for 3D and 4D MR image analysis. The authors have no doubts that the general and broad field of computer vision has much to contribute to automate the medical image analysis in general, and MR image analysis in particular.

7.7 Acknowledgments

This work was supported in part by NIH grants-R01 HL63373, R37 HL61857, American Heart Association grant 0160452Z (Heartland Affiliate), and Innovative Research Incentive 2001 grant from the Netherlands Organization for Scientific Research.

References

- [1] Bloch, F.: Nuclear induction. *Phys. Rev.* **70** (1946) 460–473
- [2] Purcell, E.M., Torrey, H.C., Pound, R.V.: Resonance absorption by nuclear magnetic moments in a solid. *Phys. Rev.* **69** (1946) 37–38
- [3] Lauterbur, P.C.: Image formation by induced local interactions: examples employing nuclear magnetic resonance. *Nature* **242** (1973) 190–191
- [4] Lanzer, P., Barta, C., Botvinick, E.H., Wiesendanger, H.U., Modin, G., Higgins, C.B.: ECG-synchronized cardiac MR imaging: method and evaluation. *Radiology* **155** (1985) 681–686
- [5] Danias, P., McConnell, M., Khasgiwala, V., Chuang, M., Edelman, R., W.J., M.: Prospective navigator correction of image position for coronary MR angiography. *Radiology* **203** (1997) 733–736

- [6] Wang, Y., Rossman, P.J., Grimm, R.C., Riederer, S.J., Ehman, R.L.: Navigator echo-based real-time respiratory gating and triggering for reduction of respiration effects in three-dimensional coronary MR angiography. *Radiology* **198** (1996) 55–60
- [7] Yang, P., Kerr, A., Liu, A., Hardy, C., Meyer, C., Macovski, A., Pauly, J., Hu, B.: New real-time interactive cardiac magnetic resonance imaging system complements echocardiography. *J. Am. Coll. Cardiol* **32** (1998) 2049–2056
- [8] Simonetti, O., Finn, J., White, R., Laub, G., Henry, D.A.: “Black blood” T2-weighted inversion recovery MR imaging of the heart. *Radiology* **199** (1999) 49–57
- [9] Atkinson, D.J., Edelman, R.R.: Cineangiography of the heart in a single breath hold with a segmented turboFLASH sequence. *Radiology* **178** (1991) 357–360
- [10] Oppelt, A., Graumann, R., Barfuss, H., Fischer, H., Hartl, W., Shajor, W.: FISP: a new fast MRI sequence. *Electromedia* **54** (1986) 15–18
- [11] Barkhausen, J., Ruehm, S.G., Goyen, M., Buck, T., Laub, G., Debatin, J.F.: MR evaluation of ventricular function: true fast imaging with steady-state precession versus fast low-angle shot cine MR imaging: feasibility study. *Radiology* **219** (2001) 264–269
- [12] Plein, S., Bloomer, T.N., Ridgway, J.P., Jones, T.R., Bainbridge, G.J., Sivananthan, M.U.: Steady-state free precession magnetic resonance imaging of the heart: comparison with segmented k -space gradient-echo imaging. *J. Magn. Reson. Imaging* **14** (2001) 230–236
- [13] Buser, P.T., Auffermann, W., Holt, W.W., Wagner, S., Kircher, B., Wolfe, C., Higgins, C.B.: Noninvasive evaluation of global left ventricular function with use of cine nuclear magnetic resonance. *J Am Coll Cardiol* **13** (1989) 1294–1300
- [14] Foo, T.K.F., Ho, V.B., Kraitchman, D.: Single breath-hold single-phase and CINE 3D acquisition using variable temporal k -space sampling. In: *Proc. ISMRM, 9th Annual Meeting, Glasgow* (2001) 112
- [15] Scheffler, K.: 3D cardiac cine imaging in a single breath-hold using elliptically reordered 3D trueFISP. In: *Proc. ISMRM, 9th Annual Meeting, Glasgow* (2001) 113
- [16] Sodickson, D., Manning, W.: Simultaneous acquisition of spatial harmonics (SMASH): fast imaging with radiofrequency coil arrays. *Magn. Reson. Med.* **38** (1997) 591–603
- [17] Weiger, M., Pruessmann, K., Boesiger, P.: Cardiac real-time imaging using SENSE. *Magn. Reson. Med.* **43** (2000) 177–184
- [18] Madore, B., Glover, G., Pelc, N.: Unaliasing by Fourier-encoding the overlaps using the temporal dimension (UNFOLD), applied to cardiac imaging and fMRI. *Magn. Reson. Med.* **42** (1999) 813–828
- [19] Osman, N., Kerwin, W., McVeigh, E., Prince, J.: Cardiac motion tracking using CINE harmonic phase (HARP) magnetic resonance imaging. *Magn. Reson. Med.* **42** (1999) 1048–1060

- [20] Lima, J.A., Judd, R.M., Bazille, A., Schulman, S.P., Atalar, E., Zerhouni, E.A.: Regional heterogeneity of human myocardial infarcts demonstrated by contrast-enhanced MRI: Potential mechanisms. *Circulation* **92** (1995) 1117–1125
- [21] Wu, K.C., Zerhouni, E.A., Judd, R.M., Lugo-Olivieri, C.H., Barouch, L.A., Schulman, S.P., Blumenthal, R.S., Lima, J.A.: Prognostic significance of microvascular obstruction by magnetic resonance imaging in patients with acute myocardial infarction. *Circulation* **97** (1998) 765–772
- [22] Kim, R.J., Fieno, D.S., Parrish, T.B., Harris, K., Chen, E.L., Simonetti, O., Bundy, J., Finn, J.P., Klocke, F.J., Judd, R.M.: Relationship of MRI delayed contrast enhancement to irreversible injury, infarct age, and contractile function. *Circulation* **100** (1999) 1992–2002
- [23] Rehwald, W.G., Fieno, D.S., Chen, E.L., Kim, R.J., Judd, R.M.: Myocardial magnetic resonance imaging contrast agent concentrations after reversible and irreversible ischemic injury. *Circulation* **105** (2002) 224–229
- [24] Brittain, J., Hu, B., Wright, G., Meyer, C., Macovski, A., Nishimura, D.: Coronary angiography with magnetization-prepared T2 contrast. *Magn. Reson. Med.* **33** (1995) 689–696
- [25] Peters, D., Korosec, F., Grist, T., Block, W., Holden, J., Vigen, K., C.A., M.: Undersampled projection reconstruction applied to MR angiography. *Magn. Reson. Med.* **43** (2000) 91–101
- [26] Taylor, A.M., Panting, J.R., Keegan, J., Gatehouse, P.D., Amin, D., Jhooti, P., Yang, G.Z., McGill, S., Burman, E.D., Francis, J.M., Firmin, D.N., Pennell, D.J.: Safety and preliminary findings with the intravascular contrast agent NC100150 injection for MR coronary angiography. *J Magn Reson Imaging* **9** (1999) 220–227
- [27] Stillman, A.E., Wilke, N., Li, D., Haacke, E.M., McLachlan, S.: Evaluation of ultrasmall superparamagnetic iron oxide to enhance magnetic resonance angiography of the renal and coronary arteries: work in progress. *J. Comput. Assist. Tomogr.* **20** (1996) 51–55
- [28] Li, D., Dolan, B., Walovitch, R., Lauffer, R.: Three-dimensional MR imaging of coronary arteries using an intravascular contrast agent. *Magn. Reson. Med.* **39** (1998) 1014–1018
- [29] Frangi, A.F., Niessen, W.J., Viergever, M.A.: Three-dimensional modeling for functional analysis of cardiac images: A review. *IEEE Trans. Med. Imaging* **20** (2001) 2–25
- [30] Vemuri, B.C., Radisavljevic, A.: Multiresolution stochastic hybrid shape models with fractal priors. *ACM Trans. on Graphics* **13** (1994) 177–207
- [31] Staib, L.H., Duncan, J.S.: Model-based deformable surface finding for medical images. *IEEE Trans. Med. Imaging* **15** (1996) 720–731
- [32] Metaxas, D.N.: *Physics-Based Deformable Models*. Kluwer, Boston MA (1996)

- [33] Metaxas, D.N., Kakadiaris, I.A.: Elastically adaptive deformable models. *IEEE Trans. Pattern Anal. and Machine Intelligence* **24** (2002) 1310–1321
- [34] Cootes, T.F., Cooper, D.H., Taylor, C.J., Graham, J.: Trainable method of parametric shape description. *Image and Vision Computing* **10** (1992) 289–294
- [35] Cootes, T.F., Taylor, C.J., Cooper, D.H., Graham, J.: Active shape models-their training and application. *Computer Vision and Image Understanding* **61** (1995) 38–59
- [36] Hill, A., Cootes, T.F., Taylor, C.J., Lindley, K.: Medical image interpretation: A generic approach using deformable templates. *Medical Informatics* **19** (1994) 47–59
- [37] Duta, N., Sonka, M.: Segmentation and interpretation of MR brain images: An improved active shape model. *IEEE Trans. Med. Imaging* **17** (1998) 1049–1062
- [38] Kelemen, A., Szekely, G., Gerig, G.: Elastic model-based segmentation of 3D neurological data sets. *IEEE Trans. Med. Imaging* **18** (1999) 828–839
- [39] Pizer, S.M., Joshi, S., Fletcher, T., Styner, M., Tracton, G., Chen, J.Z.: Segmentation of single-figure objects by deformable M-reps. In Niessen, W., Viergever, M., eds.: *MICCAI 2001*, Berlin, Springer Verlag (2001) 862–871
- [40] Stetten, G.D., Pizer, S.M.: Medial-node models to identify and measure objects in real-time 3D echocardiography. *IEEE Trans. Med. Imaging* **18** (1999) 1025–1034
- [41] Shen, D., Herskovits, E.H., Davatzikos, C.: An adaptive focus statistical shape model for segmentation and shape modeling of 3D brain structures. *IEEE Trans. Med. Imaging* **20** (2001) 257–270
- [42] Cootes, T.F., Beeston, C., Edwards, G.J., Taylor, C.J.: A unified framework for atlas matching using active appearance models. In Kuba, A., Samal, M., eds.: *Information Processing in Medical Imaging. Lecture Notes in Computer Science*, Visegrad, Hungary, Springer Verlag, Berlin (1999) 322–333
- [43] Cootes, T.F.: Statistical models of appearance for computer vision. Technical report, available at http://www.isbe.man.ac.uk/~bim/Models/app_model.ps.gz (1999)
- [44] Edwards, G., Taylor, C., Cootes, T.: Interpreting face images using active appearance models. In: *3rd International Conference on Automatic Face and Gesture Recognition 1998*, Nara, Japan (1998) 300–305
- [45] Mitchell, S.C., Lelieveldt, B.P.F., van der Geest, R.J., Bosch, H.G., Reiber, J.H.C., Sonka, M.: Cardiac segmentation using active appearance models. *IEEE Trans. Med. Imaging* **20** (2001) 415–423
- [46] Bosch, J.G., Mitchell, S.C., Lelieveldt, B.P.F., Nijland, F., Kamp, O., Sonka, M., Reiber, J.H.C.: Automatic segmentation of echocardio-

- graphic sequences by active appearance models. *IEEE Trans. Med. Imaging* **21** (2002) 1374–1383
- [47] Lelieveldt, B., Mitchell, S., Bosch, J., van der Geest, R., Sonka, M., Reiber, J.: Time-continuous segmentation of cardiac image sequences using Active Appearance Motion Models. In: *Information Processing in Medical Imaging: Lecture Notes in Computer Science*, vol. 2082, New York, Springer-Verlag (2001) 446–452
 - [48] Mitchell, S.C., Bosch, J.G., Lelieveldt, B.P.F., van der Geest, R.J., Reiber, J.H.C., Sonka, M.: 3D Active Appearance Models: Segmentation of cardiac MR and ultrasound images. *IEEE Trans. Med. Imaging* **21** (2002) 1167–1178
 - [49] Sonka, M., Hlavac, V., Boyle, R.: *Image Processing, Analysis, and Machine Vision*. 2nd edn. PWS, Pacific Grove, CA (1998)
 - [50] Goodall, C.: Procrustes methods in the statistical analysis of shape. *J. Royal Stat. Soc. B* **53**(2) (1991) 285–339
 - [51] Bookstein, F.L.: *Morphometric Tools for Landmark Data*. Cambridge University Press, Cambridge, MA (1991)
 - [52] Altmann, S.: *Rotations, Quaternions and Double Groups*. Clarendon Press, Oxford, England (1986)
 - [53] Besl, P.J., McKay, N.D.: A method for registration of 3D shapes. *IEEE Trans. Pattern Anal. and Machine Intelligence* **14** (1992) 239–256
 - [54] Cootes, T.F., Edwards, G.J., Taylor, C.: Active appearance models. *IEEE Trans. Pattern Anal. and Machine Intelligence* **23** (2001) 681–685
 - [55] Baker, S., Matthews, I.: Equivalence and efficiency of image alignment algorithms. In: *Computer Vision and Pattern Recognition Conference*. Volume 1. (2001) 1090–1097
 - [56] van der Geest, R.J., Buller, V.G.M., Jansen, E., Lamb, H.J., Baur, L.H.B., van der Wall, E.E., de Roos, A., Reiber, J.H.C.: Comparison between manual and semiautomated analysis of left ventricular volume parameters from short-axis MR images. *Journal of Computer-Assisted Tomography* **21** (1997) 756–765
 - [57] Jacob, G., Noble, A., Mulet-Parada, M., Blake, A.: Evaluating a robust contour tracker on echocardiographic sequences. *Medical Image Analysis* **3** (1999) 63–75
 - [58] Montagnat, J., Sermesant, M., Delingette, H., Malandain, G., Ayache, N.: Anisotropic filtering for model-based segmentation of 4D cylindrical echocardiographic images. *Pattern Recognition Letters* **24** (2003) 815–828
 - [59] Hamarneh, G., Gustavsson, T.: Deformable spatio-temporal shape models: Extending ASM to 2D+Time. In: *12th British Machine Vision Conference*. (2001) 13–22
 - [60] Barillot, C., Gibaud, B., Scarabin, J., Coatrieux, J.: 3D reconstruction of cerebral blood vessels. *IEEE Computer Graphics Applications* (1985) 13–19

- [61] Vignaud, J., Rabischong, P., Yver, J.P., Pardo, P., Thurel, C.: Multi-directional reconstruction of angiograms by stereogrammetry and computer: Application to computed tomography. *Neuroradiology* **18** (79) 1–7
- [62] Fessler, J., Macovski, A.: Object-based 3D reconstruction of arterial trees from magnetic resonance angiograms. *IEEE Trans. Med. Imaging* **10** (1991) 25–39
- [63] Garreau, M., Coatrieux, J., Collorec, R., Chardenon, C.: A knowledge-based approach for 3D reconstruction and labeling of vascular networks from biplane angiographic projections. *IEEE Trans. Med. Imaging* **10** (1991) 122–131
- [64] Suetens, P.: 3D reconstruction of the blood vessels of the brain from a stereoscopic pair of subtraction angiograms. *Image and Vision Computing* **1** (1983) 43–51
- [65] Wink, O., Niessen, W., Viergever, M.: Fast quantification of abdominal aortic aneurysms from cta volumes. In: *Medical Image Conference and Computer-Assisted Interventions (MICCAI'98)*, Berlin, Springer-Verlag (1998) 138–145
- [66] Masutani, Y., Schiemann, T., Hohne, K.: Vascular shape segmentation and structure extraction using a shape-based region-growing model. In: *MICCAI '98, First International Conference on Medical Image Computing and Computer-Assisted Intervention*, Boston, MA, Springer-Verlag, New York (1998) 1242–1249
- [67] Lobregt, S., Verbeek, P.W., Groen, F.C.A.: Three-dimensional skeletonization. *IEEE Transactions on Pattern Analysis and Machine Intelligence* **2** (1980) 75–77
- [68] Saha, P.K., Chaudhuri, B.B., Chandra, B., Majumder, D.D.: Topology preservation in 3D digital space. *Pattern Recognition* **27** (1994) 295–300
- [69] Higgins, W., Spyra, W., Ritman, E.: System for analyzing high-resolution three-dimensional coronary angiograms. *IEEE Trans. Med. Imaging* **15** (1996) 377–385
- [70] Pizer, S.M., Eberly, D.H., Morse, B.S., Fritsch, D.S.: Zoom invariant vision of figural shape: The mathematics of cores. *Computer Vision and Image Understanding* **69** (1998) 55–71
- [71] Morse, B.S., Pizer, S.M., Liu, A.: Multiscale medial analysis of medical images. *Proceedings on Information Processing in Medical Images* **687** (1993) 112–131
- [72] Furst, J., Pizer, S.M., Eberly, D.: Marching cores: A method for extracting cores from 3d medical images. In: *Proceedings of the Workshop on Mathematical Models in Biomedical Image Analysis*, IEEE Computer Society Technical Committee on Pattern Analysis and Machine Intelligence (1996) 124–130
- [73] Lorigo, L.M., Faugeras, O.D., Grimson, W.E.L., Keriven, R., Kikinis, R., Nabavi, A., Westin, C.F.: CURVES: Curve evolution for vessel segmentation. *Medical Image Analysis* **5** (2001) 195–206

- [74] Sethian, J.A.: *Level Set Methods*. Cambridge University Press, Cambridge, MA (1996)
- [75] Sapiro, G.: Vector-valued active contours. In: *Proc. of Computer Vision and Pattern Recognition*, Los Alamitos, CA, IEEE Comp. Soc. (1996) 680–685
- [76] Caselles, V., Kimmel, R., Sapiro, G.: Geodesic active contours. *Int. J. of Comp. Vision* **22** (1997) 61–79
- [77] Carpenter, J.P., Owen, R.S., Holland, G.A., Baum, R.A., Barker, C.F., Perloff, L.J., Golden, M.A., Cope, C.: Magnetic resonance angiography of the aorta, iliac, and femoral arteries. *Surgery* **116** (1994) 17–23
- [78] Evans, A.J., Sostman, H.D., Knelson, M.H., Spritzer, C.E., Newman, G.E., Paine, S.S., Beam, C.A.: Detection of deep venous thrombosis: Prospective comparison of MR imaging with contrast venography. *Am J Radiology* **161** (131–139) 1993
- [79] Spritzer, C.E.: Venography of the extremities and pelvis. *Magn Reson Imag Clinics of North Amer* **1** (1993) 239–251
- [80] Smedby, O.: Visualizations of arteries and veins with 3D image processing methods. In: *XI International Workshop on Magnetic Resonance Angiography: New Aspects on Visualisation of Macro- and Microcirculation*. (1999) 102
- [81] Lei, T., Udupa, J.K., Saha, P.K., Odhner, D.: Artery-vein separation via MRA-An image processing approach. *IEEE Trans. Med. Imaging* **20** (2001) 689–703
- [82] Fritsch, D.S., Eberly, D., Pizer, S.M., McAuliffe, M.J.: Stimulated cores and their applications in Medical imaging. In: *Information Processing in medical Imaging*, Berlin, Springer-Verlag (1995) 365–368
- [83] Aylward, S., Pizer, S.M., Bullitt, E., Eberly, D.: Intensity ridge for tubular object segmentation and description. In: *Proc. Workshop on Mathematical Methods in Biomedical Image Analysis*, IEEE Catalog 96TB100056, IEEE (1996) 131–138
- [84] Bullitt, E., Aylward, S., Liu, A., Stone, J., Mukherji, S.K., Coffey, C., Gerig, G., Pizer, S.M.: 3D graph description of the intracerebral vasculature from segmented MRA and tests of accuracy by comparison with x-ray angiograms. In Kuba, A., Samal, M., Todd-Pokropek, A., eds.: *Information Processing in Medical Imaging*. Springer-Verlag, Berlin (1999) 308–321
- [85] Stefancik, R.M., Sonka, M.: Highly automated segmentation of arterial and venous trees from three-dimensional MR angiography. *Int. J. Card. Imag.* **17** (2001) 37–47
- [86] Sonka, M., Hlavac, V., Boyle, R.: *Image Processing, Analysis, and Machine Vision*. 2nd edn. PWS, Pacific Grove, CA (1998) (1st edition Chapman and Hall, London, 1993).
- [87] Stefancik, R.M.: Segmentation of arteries and veins in contrast-enhanced magnetic resonance angiography using a graph-search technique. Master's thesis, The University of Iowa (1999)

- [88] Udupa, J.K., Wei, L., Samarasekera, S., Miki, Y., van Buchem, M.A., Grossman, R.I.: Multiple sclerosis lesion quantification using fuzzy-connectedness principles. *IEEE Trans. Med. Imaging* **16** (1997) 598–609
- [89] Rice, B.L., Udupa, J.K.: Fuzzy-connected clutter-free volume rendering for MR angiography. *International Journal of Imaging Systems and Technology* **11** (2000) 62–70
- [90] Saha, P.K., Udupa, J.K., Odhner, D.: Scale-based fuzzy connected image segmentation: Theory, algorithms, and validation. *Computer Vision and Image Understanding* **77** (2000) 145–174
- [91] Noeske, R., Seifert, F., Rhein, K.H., Rinneberg, H.: Human cardiac imaging at 3 T using phased array coils. *Magnetic Resonance in Medicine* **44** (2000) 978–982
- [92] Yang, Y., Gu, H., Zhan, W., Xu, S., Silbersweig, D.A., Stern, E.: Simultaneous perfusion and BOLD imaging using reverse spiral scanning at 3T: characterization of functional contrast and susceptibility artifacts. *Magnetic Resonance in Medicine* **48** (2002) 278–289
- [93] Fayad, Z.A., Fuster, V.: Characterization of atherosclerotic plaques by magnetic resonance imaging. *Annals of the New York Academy of Sciences*. **902** (2000) 173–86
- [94] Fuster, V., ed.: *The Vulnerable Atherosclerotic Plaque: Understanding, Identification, and Modification*. American Heart Association. Futura publishing company, Armonk, New York (1999)
- [95] Touissant, J.F., LaMuraglia, G.M., Southern, J.F.: Magnetic resonance images lipid, fibrous, calcified, hemorrhagic, and thrombotic components of human atherosclerosis in vivo. *Circulation* **94** (1996) 932–938
- [96] Shinnar, M., Fallon, J., Wehrli, S., Levin, M., Dalmacy, D., Fayad, Z., Badimon, J., Harrington, M., Harrington, E., Fuster, V.: The diagnostic accuracy of ex vivo MRI for human atherosclerotic plaque characterization. *Arteriosclerosis, Thrombosis & Vascular Biology* **19** (1999) 2756–2761
- [97] Yuan, C., Mitumori, L.M., Ferguson, M.S., Polissar, N.L., Echelard, D., Ortiz, G., Small, R., Davies, J.W., Kerwin, W.S., Hatsukami, T.S.: In vivo accuracy of multispectral magnetic resonance imaging for identifying lipid-rich necrotic cores and intraplaque hemorrhage in advanced human carotid plaques. *Circulation*. **104** (2001) 2051–6
- [98] Yuan, C., Hatsukami, T.S., Obrien, K.D.: High-resolution magnetic resonance imaging of normal and atherosclerotic human coronary arteries ex vivo: discrimination of plaque tissue components. *Journal of Investigative Medicine*. **49** (2001) 491–9
- [99] Yuan, C., Zhang, S.X., Polissar, N.L., Echelard, D., Ortiz, G., Davis, J.W., Ellington, E., Ferguson, M.S., Hatsukami, T.S.: Identification of fibrous cap rupture with magnetic resonance imaging is highly associated with recent transient ischemic attack or stroke. *Circulation*. **105** (2002) 181–5

- [100] Yuan, C., Kerwin, W.S., Ferguson, M.S., Polissar, N., Zhang, S., Cai, J., Hatsukami, T.S.: Contrast-enhanced high resolution MRI for atherosclerotic carotid artery tissue characterization. *J. Mag. Res. Imaging*. **15** (2002) 62–7
- [101] Serfaty, J.M., Chaabane, L., Tabib, A., Chevallier, J.M., Briguet, A., Douek, P.C.: Atherosclerotic plaques: classification and characterization with t2-weighted high-spatial-resolution MRI imaging: an in vitro study. *Radiology*. **219** (2001) 403–10
- [102] Coombs, B.D., Rapp, J.H., Ursell, P.C., Reilly, L.M., Saloner, D.: Structure of plaque at carotid bifurcation: High-resolution MRI with histological correlation. *Stroke* **32** (2001) 2516–2521
- [103] Hatsukami, T.S., Ross, R., Polissar, N.L., Yuan, C.: Visualization of fibrous cap thickness and rupture in human atherosclerotic carotid plaque in vivo with high-resolution magnetic resonance imaging. *Circulation* **102** (2000) 959–964
- [104] Sonka, M., Thedens, D.R., Schulze-Bauer, C., Holzapfel, G., Stollberger, R., Bolinger, L., Wahle, A.: Towards MR assessment of plaque vulnerability: Image acquisition and segmentation. In: 10th Scientific Meeting of the International Society for Magnetic Resonance in Medicine, Berkeley, CA, ISMRM (2002) 1570
- [105] Brejl, M., Sonka, M.: Object localization and border detection criteria design in edge-based image segmentation: Automated learning from examples. *IEEE Trans. Med. Imaging* **19** (2000) 973–985
- [106] Holzapfel, G.A., Schulze-Bauer, C.A.J., Stadler, M.: Mechanics of angioplasty: Wall, balloon and stent. In: *Mechanics in Biology*. J Casey and G Bao (Eds.), New York, The American Society of Mechanical Engineers (ASME) (2000) AMD-Vol. 242/BED-Vol. 46, 141–156.